AGU PUBLICATIONS

JGR

Journal of Geophysical Research: Atmospheres

RESEARCH ARTICLE
10.1002/2017JD026526

Influences of the MJO on the space-time organization of tropical convection

Juliana Dias[1,2], **Naoko Sakaeda**[2], **George N. Kiladis**[2], **and Kazuyoshi Kikuchi**[3]

[1]CIRES, University of Colorado Boulder, Boulder, Colorado, USA, [2]Physical Sciences Division, NOAA Earth System Research Laboratory, Boulder, Colorado, USA, [3]International Pacific Research Center, School of Ocean and Earth Science and Technology, University of Hawaii, Honolulu, Hawaii, USA

Abstract The fact that the Madden-Julian Oscillation (MJO) is characterized by large-scale patterns of enhanced tropical rainfall has been widely recognized for decades. However, the precise nature of any two-way feedback between the MJO and the properties of smaller-scale organization that makes up its convective envelope is not well understood. Satellite estimates of brightness temperature are used here as a proxy for tropical rainfall, and a variety of diagnostics are applied to determine the degree to which tropical convection is affected either locally or globally by the MJO. To address the multiscale nature of tropical convective organization, the approach ranges from space-time spectral analysis to an object-tracking algorithm. In addition to the intensity and distribution of global tropical rainfall, the relationship between the MJO and other tropical processes such as convectively coupled equatorial waves, mesoscale convective systems, and the diurnal cycle of tropical convection is also analyzed. The main findings of this paper are that, aside from the well-known increase in rainfall activity across scales within the MJO convective envelope, the MJO does not favor any particular scale or type of organization, and there is no clear signature of the MJO in terms of the globally integrated distribution of brightness temperature or rainfall.

Key Points:
- The MJO aggregates tropical convection without altering either its integrated global distribution or organization characteristics
- Higher-frequency convective variability is enhanced within the MJO convective phase
- MJO convective and suppressed regions do not favor any particular smaller-scale modes of tropical variability

Correspondence to:
J. Dias,
juliana.dias@noaa.gov

Citation:
Dias, J., N. Sakaeda, G. N. Kiladis, and K. Kikuchi (2017), Influences of the MJO on the space-time organization of tropical convection, *J. Geophys. Res. Atmos.*, *122*, 8012–8032, doi:10.1002/2017JD026526.

Received 18 JAN 2017
Accepted 11 JUL 2017
Accepted article online 17 JUL 2017
Published online 14 AUG 2017

1. Introduction

The Madden-Julian Oscillation (MJO) is the leading mode of intraseasonal variability in the tropics. It is characterized by a coherent eastward moving planetary-scale signal that can be seen in many variables, from the atmospheric circulation to deep convection. The convectively active phase of the MJO peaks over the Indo-Pacific region, and it is made up of a wide variety of smaller-scale convective disturbances that, on average, appear to develop and decay within the large-scale MJO convective envelope as it shifts toward the east [*Nakazawa*, 1988; *Hendon and Liebmann*, 1994; *Masunaga et al.*, 2006; *Kikuchi and Wang*, 2010]. This wide range of organized tropical phenomena associated with the MJO includes the diurnal cycle of precipitation and other sub-MJO scale disturbances such as Kelvin waves, inertio-gravity waves, easterly waves, tropical storms, and mesoscale convective systems (MCSs). All of these entities can occur independently of the MJO, which raises the main question addressed in this paper: How does the presence, absence, or strength of the MJO relate to the variability and characteristics of smaller-scale tropical phenomena? Our focus is not only on how the MJO active phase interacts locally with smaller-scale tropical processes, but we are also interested in whether there are detectable signals of the MJO over the global tropics as a whole. We take an observational approach to address these issues, where our starting point is to identify MJO convective envelopes and a measure of MJO activity. Next, we use a variety of methodologies to diagnose organized tropical convection at smaller scales that are then conditioned on the statistics of the MJO, both locally and remotely.

From a theoretical standpoint, determining how the MJO is related to other tropical phenomena may improve our understanding of its driving mechanisms and impacts. For instance, if there are specific modes of higher-frequency variability that are more prominent within certain phases of the MJO, it is possible that those are necessary ingredients for its initiation, maintenance, and/or propagation. In contrast, the lack of a relationship between the MJO and smaller-scale convective organization supports the idea that the MJO is an independent mode of variability that primarily provides a background that is more or less favorable to other moist convective processes, without necessarily organizing those processes in any particular way. Determining the relationship between the MJO and smaller-scale convective organization also has important modeling implications. For example, as climate models are run at higher resolutions and physical parametrizations are

improved in order to better resolve the MJO convective envelope, it is important to identify whether the observed relationships with higher-frequency variability are also being properly simulated. On one hand, it is possible that if there is a strong relationship between the MJO and smaller-scale convective organization, then a model's ability to represent intraseasonal variability might be closely tied to how, for example, the diurnal cycle of tropical rainfall or smaller-scale tropical waves are represented [e.g., *Guo et al.*, 2015]. On the other hand, if there is no systematic relationship beyond modulations of the amplitude of the disturbances that make up the MJO, then it is possible that a climate model's MJO skill can be improved independently of the model's ability to reproduce the entire spectrum of tropical convective variability.

While there are certainly many other important atmospheric phenomena that have been shown to be affected by the MJO [*Zhang*, 2013], our focus here is on the relationship between tropical convective processes that are organized at scales smaller than the MJO. We start by investigating the relationship between the MJO and the general distribution of tropical convection. In a climatological sense, intense convective activity is restricted to relatively small geographical regions (e.g., the western Pacific warm pool and the Intertropical Convergence Zone) that are surrounded by much drier regions. This behavior is reflected by the negatively skewed probability density function (pdf) of tropical satellite brightness temperature (T_b) that is shown in section 3. Clear skies (e.g., warm T_b) limit the right tail of the pdf, whereas the cold temperatures within the left tail are associated with deep convection. It is expected that the frequency of occurrence of low T_b would be increased (reduced) within the MJO convective (suppressed) envelope. One of our goals is to quantify these changes and to determine whether the MJO impacts the global tropical pdf of T_b. Simply stated, we are interested in the question *Are periods of intense MJO activity associated with a change in total tropical rainfall, or does the MJO simply act to redistribute convective activity in space without affecting total tropical rainfall amounts?* The remainder of the paper focuses on whether the space-time organization of tropical convection is sensitive to the MJO either locally or remotely.

The first type of tropical disturbances we investigate are the so called convectively coupled equatorial waves (CCEWs). CCEWs are synoptic-scale disturbances that can be identified in tropical cloudiness satellite data [*Takayabu*, 1994; *Wheeler and Kiladis*, 1999; *Wheeler et al.*, 2000; *Kiladis et al.*, 2009] and that share many similarities with the theoretical shallow water equatorial modes of *Matsuno* [1966], including dispersion characteristics, equatorially trapped spatial structures, and zonal propagation. The relationship between the MJO and CCEWs has been investigated in many earlier studies [e.g., *Nakazawa*, 1988; *Hendon and Liebmann*, 1994; *Roundy and Frank*, 2004; *Masunaga et al.*, 2006; *Roundy*, 2008; *Yasunaga*, 2011; *Dias et al.*, 2013; *Guo et al.*, 2015]. For example, *Roundy* [2008] suggest that Kelvin waves propagate more slowly inside compared to outside the MJO convective envelope, and *Yasunaga* [2011] suggests an amplitude enhancement of all CCEWs within the convective phase of the MJO, except for MRGs. In addition, *Dias et al.* [2013] showed that there is only a very weak systematic relationship between the dispersion characteristics of CCEWs and the MJO phase, which is consistent with the relative insensitivity of CCEWs to zonal variations of the basic state [*Dias and Kiladis*, 2014]. Here our focus is on, besides local effects, whether the MJO changes the global total CCEW variance as well as on the potential influence of background variability on these relationships.

The second class of disturbances we discuss is tropical mesoscale convective systems (MCSs). This work builds on the object-tracking approach of *Dias et al.* [2012], where mesoscale cloudiness areas are identified as objects defined by connected regions of T_b below a given threshold. As shown in *Dias et al.* [2012], most of these features last for less than a day, span a few hundred kilometers, and they make up the convective envelopes of CCEWs and the MJO. One interesting result from *Dias et al.* [2012] is that the morphology of these mesoscale cloudiness features is fairly robust to the T_b threshold used to define them. That implies that in regions where low T_b is more frequent, such as within the MJO convective envelope, one might expect that more objects would be detected as opposed to detecting larger objects or longer lasting ones. Aside from testing this hypothesis, other questions that we address are related to whether the MJO affects MCS propagation characteristics and life span and, if so, whether such changes are local or global.

Lastly, we investigate the effects of the MJO on the diurnal cycle of tropical convection. The relationship between diurnal cycle of tropical convection and the MJO has been studied mostly from a local point of view, and while there have been some discrepancies in their conclusions, studies tend to agree that the amplitude of the diurnal cycle is enhanced during the convective active phase of the MJO (see discussions in *Oh et al.* [2011], *Peatman et al.* [2014], and *Sakaeda et al.* [2017]). Our focus here is on the specific question of whether the diurnal cycle amplitude and phase of tropical convection on a global scale is affected by MJO activity. It

turns out that the relationship between the MJO and the diurnal cycle of tropical rainfall, and in particular its diurnal phase, is very complex; thus, we refer to *Sakaeda et al.* [2017] for a more in depth analysis of this aspect.

Throughout the paper we present a parallel analysis from a local MJO standpoint to identify MJO convective versus suppressed regions, and from a global standpoint to identify periods of weak versus strong MJO activity. The outline is as follows: in section 2, data sets and methodology are described. The following sections deal with assessing how the MJO relates to the distribution of tropical convection (section 3), CCEW variance (section 4), mesoscale convective organization (section 5), and the diurnal cycle of tropical convection (section 6). In the final section the main results are summarized and their implications in view of theories of the MJO are discussed.

2. Data and Methodology

2.1. Data

The Cloud Archive User Service (CLAUS) data set [*Hodges et al.*, 2000] along with the globally merged infrared radiation (IR) data set [*Janowiak et al.*, 2001] is used throughout the paper. CLAUS T_b estimates extend from 1 July 1983 through 30 June 2009 at 8 times daily resolution on a 0.5° × 0.5° horizontal grid. IR T_b estimates begin on 18 September 1999 and are reported at 48 times daily and 4 km ×4 km in the horizontal. IR data was regridded and calibrated to CLAUS T_b using the 1999 through 2009 overlap period, and these recalibrated IR data were appended to the CLAUS data set starting on 1 July 2009. The calibration consists of adjusting the mean and standard deviation of regridded IR T_b to the CLAUS T_b mean and standard deviation for the overlap period at each grid point, resulting in an 8 times daily data set extending from 1 July 1983 through 31 December 2013 on the original CLAUS grid. This merged data set is denoted CLAUS-IR. The reason why the two data sets are merged is to have a long record of high-resolution T_b and therefore more robust statistics. All of our results have been tested with CLAUS and IR data separately, as well as with precipitation estimates from the Tropical Rainfall Measuring Mission (TRMM) [*Huffman et al.*, 2007]. When high temporal resolution is not necessary (sections 3 and 4) results were also compared to the NOAA twice daily interpolated Outgoing Longwave Radiation (OLR) data set [*Liebmann and Smith*, 1996]. A few of the statistically significant differences reported in the next sections are not significant in other shorter data sets. Except for these less stable statistics, the results reported here are robust across the data sets tested.

The MJO and CCEW filtered data sets utilize the filtering technique from *Kiladis et al.* [2009], with some minor changes in the spectral coefficients used for each mode (see Table 1). Briefly, the filtering consists of an inversion of the Fourier transformed data in longitude and time-space, where all the spectral coefficients outside the ranges shown in Table 1 are set to zero. These data sets are denoted $T_{b\mathrm{MJO}}$ for MJO filtered T_b, and $T_{b\mathrm{KW}}$ for Kelvin wave, $T_{b\mathrm{EIG}}$ and $T_{b\mathrm{WIG}}$ for eastward and westward inertia gravity, $T_{b\mathrm{MRG}}$ for mixed Rossby gravity (MRG), and $T_{b\mathrm{ER}}$ for equatorial Rossby wave filtered T_b. We also include a synoptic band filter for 2–30 day variability and all wave numbers, and two additional filtering bands that do not overlap with any CCEW in order to evaluate the impact of background noise. These bands are also shown in Table 1 and are denoted $T_{b\mathrm{SYN}}$, $T_{b\mathrm{NOISEe}}$, and $T_{b\mathrm{NOISEw}}$.

Identifying the MJO is a challenge by itself as can be inferred from the large number of diverse detection methods that have been developed since its discovery [see *Straub*, 2013, and references therein]. Here the MJO convective region is determined based on $T_{b\mathrm{MJO}}$ anomalies, where the MJO active (suppressed) envelopes are defined as enclosed regions of strong negative (positive) $T_{b\mathrm{MJO}}$ anomalies. To identify global MJO activity, we use the all-season OLR-based MJO index (OMI), which is a bivariate MJO index that relies only on OLR [*Kiladis et al.*, 2014]. We primarily use OMI as opposed to the more commonly used Real-time Multivariate MJO (RMM) index of *Wheeler and Hendon* [2004] because by design it is more related to the MJO convective signal than RMM, which primarily represents MJO-related circulation [*Straub*, 2013; *Kiladis et al.*, 2014]. Because most of our analysis involves T_b thresholds, we focus on the December-January-February (DJF) season to avoid sampling seasonal biases.

2.2. Methodology

The starting point of our analysis is to sort the data set of interest conditionally on various metrics for the MJO depending on whether we are interested in local or global MJO relationships. As mentioned earlier, the MJO convective (suppressed) envelope is defined as regions in space and time where $T_{b\mathrm{MJO}}$ is below (above)

Table 1. MJO and CCEWs Spectral Filtering Regions, Where k Stands for Planetary Wave Number, ω Is the Frequency in Cycles Per Day, and h_{eq} Is the Equivalent Depth in Meters (see *Kiladis et al.* [2009] for Details)[a]

	k	ω	h_{eq}
MJO	1–8	1/96–1/30	–
KW	1–15	0.05–0.4	8–90
EIG	0–15	0.2–0.55	12–50
WIG	−15 to −1	0.35–0.8	12–90
MRG	−10 to −1	–	8–90
ER	−10 to −1	0.025–0.1	1–90
SYN	–	0.033–0.5	–
NOISEe	1– 15	0.62–0.8	–
NOISEw	−15 to −3	0.3–0.4	–

[a]Positive (negative) k corresponds to modes with eastward (westward) phase speeds.

a threshold. That is, at any gridded latitude, longitude and time (m, n, k), if T_{bMJO} (m, n, k) is below a choice of negative threshold, then the space-time location (m, n, k) is tagged as part of a MJO convective envelope (CE), and the subset of (m, n, k) that meet this criteria makes up the space-time region denoted "MJO CE." Likewise, all (m, n, k) where T_{bMJO} (m, n, k) is above a given positive threshold make up the MJO suppressed envelope subset ("MJO SE"). Figure 1 illustrates this decomposition where regions enclosed by blue (red) contours define the MJO CE (SE). Comparing dashed and solid contours in Figure 1 illustrates how the precise decomposition depends on the choice of threshold. This sensitivity is further illustrated in Figure 2, which shows for each grid point the number of DJF time stamps that belong to MJO CE (a, c, e) and MJO SE (b, d, f) for some different choices of T_{bMJO} threshold. Figure 2 demonstrates that, in addition to the specific boundaries of MJO CE and SE, the threshold also impacts the geographic distribution of MJO CE and SE. For instance, the more strict threshold (Figures 2a and 2b) are associated with data points primarily over the Indian Ocean and Maritime Continent, whereas for the less strict threshold (Figures 2e and 2f) data points are more spread out. Because sample sizes are smaller for more strict thresholds, we primarily show results using threshold defined by the 15th (85th) percentile of the global T_{bMJO} between 15°S and 15°N, and we discuss sensitivities to this choice when necessary. An MJO neutral (MJO NE) subset is used in section 4 and is defined as grid points where either

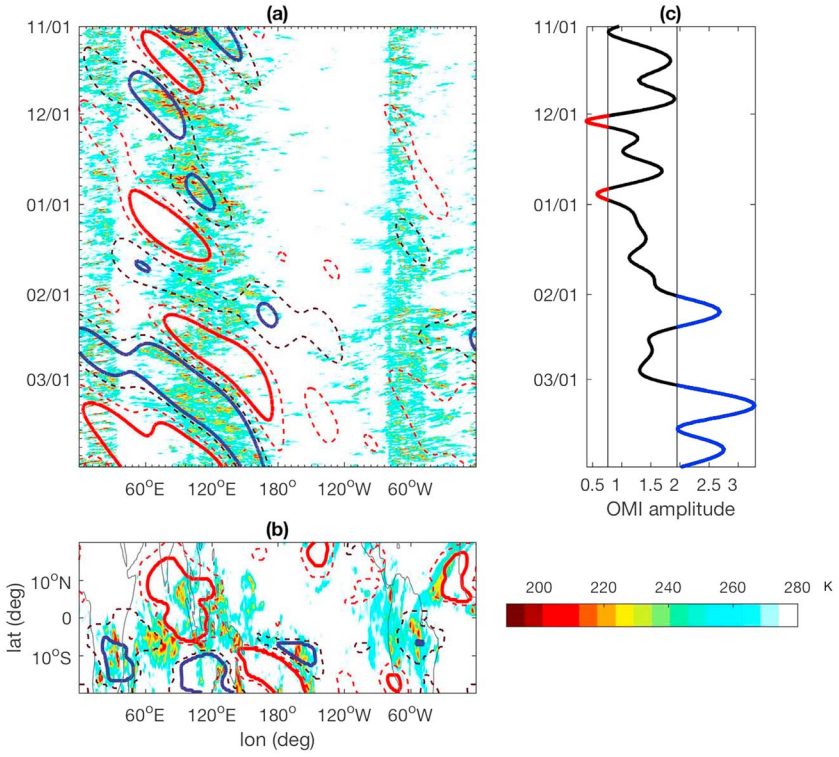

Figure 1. (a) Time-longitude cross section of CLAUS-IR T_b (shading) and T_{bMJO} (contours) at the equator. (b) Map of T_b and T_{bMJO} on 1 January 2012. Solid blue and red contours are at ±6 K, and dashed blue and red contours are at ±3 K. (c) OMI activity for the same period as in Figure 1 where the black straight lines show the 15th and 85th percentile values of OMI, and times where OMI is above (below) the 85th (15th) percentiles are shown in blue (red).

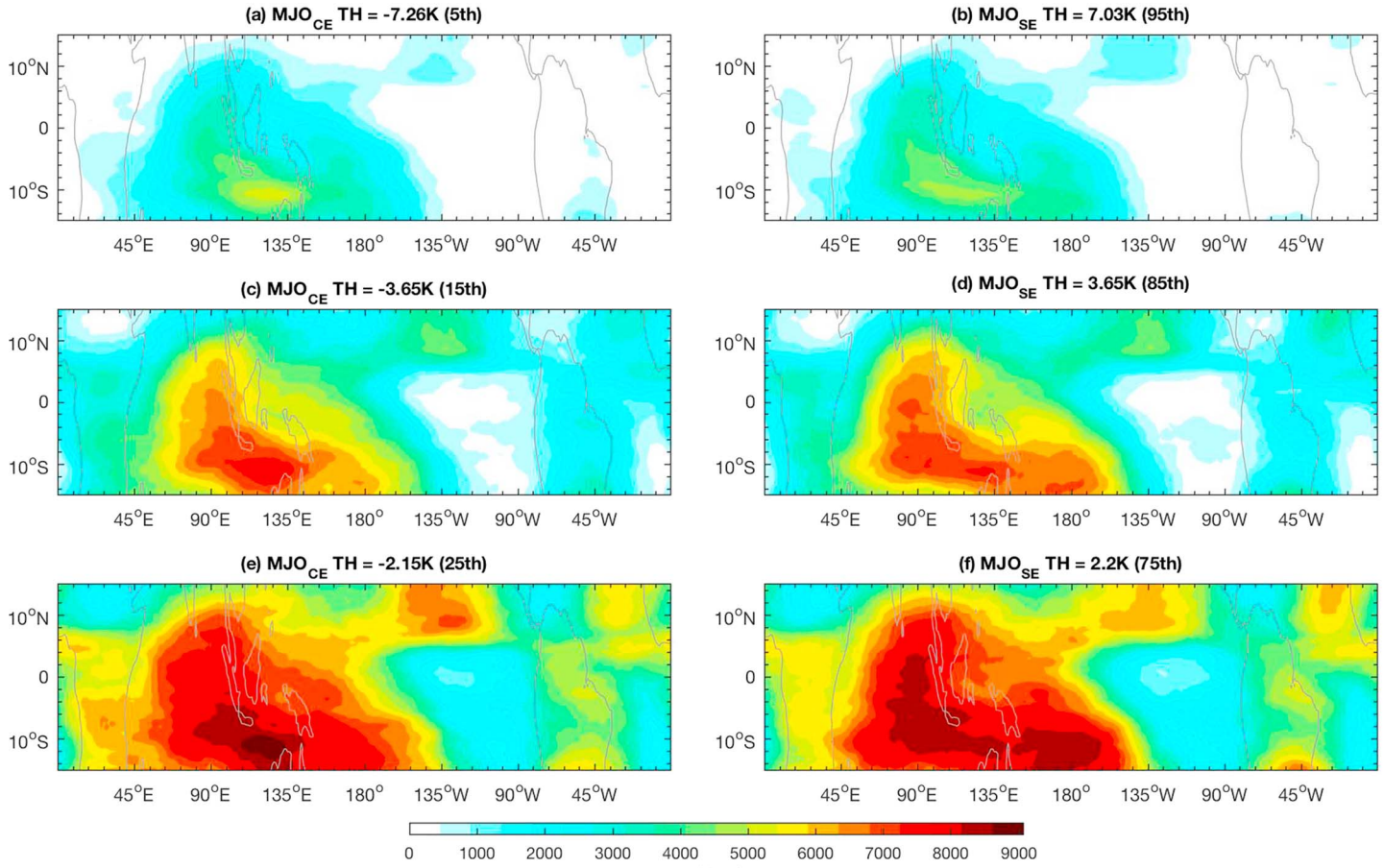

Figure 2. All panels show maps of the number of DJF data points that fall within (a, c, e) MJO convective envelopes (MJO CE) (b, d, f) and MJO suppressed envelopes (MJO SE). Each panel from top to bottom corresponds to a different choice of threshold that defines the MJO envelopes, which are displayed in each panel title.

positive or negative T_{bMJO} lies within the 15th percentile of its amplitude and is located in the Indo-Pacific region defined as the area between 50°E and 160°E and from 15°S to 5°N, in order to include only the region where the MJO is most active.

To investigate potential MJO impacts on global tropical convection, MJO activity is defined based on OMI amplitude. This method is based on time sorting exclusively, in order to investigate whether the MJO impacts convective organization in the tropics in general, including regions remote from its local convective/suppressed envelopes. Similar to the MJO CE and SE space-time decomposition, all horizontal grid points (m, n) at times when OMI is above a high threshold make up the MJO active subset (MJO A), and all horizontal grid points (m, n) when OMI is below a low threshold make up the MJO inactive subset (MJO I). The method is illustrated in Figure1c where thresholds defined by the 15th and 85th percentiles of OMI during DJF are highlighted. We note that in this data selection all grid points (m, n) between 15°S and 15°N are always included. All results shown are based on these threshold values, and sensitivities are discussed when necessary.

Based on the space-time decomposition described above, any given data set (gridded in the same way as T_{bMJO}) can be partitioned according to whether their grid point values lie in MJO CE, in MJO SE, or neither, or temporally split based on whether their time stamps lie in MJO A, MJO I, or neither. After decomposing the data set of interest, our approach is to calculate conditional statistics (means, variances, etc.) within each of these subsets, which are then compared to unconditional statistics (climatology) using all the data. Once again, all calculations are done for individual seasons to minimize seasonal biases, and we here present results for DJF only. Throughout the manuscript, statistical significance is determined using a Monte Carlo method without replacement where we randomly choose one thousand subsamples of the entire data record. This is out of 89136 samples (~30 years × 8 × daily = 89136) at each 0.5° grid point. Then, the quantity of interest,

for example, variance, is calculated in each random sample, and the 95% confidence interval (CI) is based on the 2.5th and 97.5th percentiles of that distribution. This method is used when comparing pdfs where the percentile CI is calculated for each bin. While the statistical significance of the results shown here are not particularly sensitive to binning or the choice of random samples without versus with replacement, we also use the two-sample Kolmogorov-Smirnov test (kstest) [*Massey*, 1951]. The kstest is typically used to quantify the difference between the distributions of two-sample data, using their cumulative distribution functions (cdfs). Specifically, the kstest null hypothesis is that two data samples come from the same distribution versus the alternative hypothesis that the empirical cdfs are not the same. The effective sample size is determined based on the decorrelation in time and space for each data set (more specific details are outlined in the next sections).

3. The MJO and the Distribution of Tropical Convection

This section focuses on whether the MJO shifts and/or alters the shape of the T_b pdf, whether these potential changes are local to the MJO convective regions, and whether there are global changes as well. A histogram method is used to estimate pdfs, and two approaches for normalization were initially tested. In the first method, we start by normalizing to unit area each latitude-longitude grid point histogram and then we calculate the global area weighted average (denoted "mean pdf"). In the second method the pdf is estimated by first creating a single histogram at each latitude using data from all longitudes, then weighting these latitudinal histograms by area, and then normalizing these to have unit area (denoted "aggregated pdf"). The two methods yield nearly identical pdfs (not shown) and from here on we use the aggregated pdf method. To assess the statistical significance of the differences among pdfs, we use the kstest described earlier and the random sample method described in the previous section.

The black curve in Figure 3a shows the tropical T_b pdf (pdf_{TROP}), which is estimated using all DJF data from 0°–360° to 15°S–15°N and illustrates the single peaked skewed distribution discussed in section 1. Using the data partition described in the previous section, the blue and red curves correspond to the conditional pdfs on MJO CE ($pdf_{MJO_{CE}}$) and MJO SE ($pdf_{MJO_{SE}}$), respectively. Note that the left tail of $pdf_{MJO_{CE}}$ is significantly above the tail of pdf_{TROP}, demonstrating that low T_b values are more likely to occur within the MJO CE than elsewhere in the tropics. However, relating local MJO conditional pdfs to the tropical pdf is not necessarily a fair comparison because most of the MJO CE and MJO SE data points lie within the Indo-Pacific sector which favors low T_b climatologically (Figure 2). For this reason, in order to assess the local effects of the MJO on the T_b distribution, we also compare the MJO conditional pdfs to the "local" T_b pdf. We tested a few different ways of defining the local climatological pdf, and it turns out that a simple regionally averaged pdf is very similar to the conditional pdf on MJO NE. Specifically, the dashed black line in Figure 3a shows the DJF T_b pdf for the Indo-Pacific region defined in the previous section (pdf_{IP}), which is roughly the region where MJO CE and SE are most likely to occur. The left tail of pdf_{IP} is above pdf_{TROP}, showing that low T_b are more likely to occur in the Indo-Pacific sector in comparison to the global tropics, but it is significantly below $pdf_{MJO_{CE}}$ (shading correspond to the 95% CI at each bin). Similarly, the $pdf_{MJO_{SE}}$ shows a small decrease in the probability of low T_b values within MJO SE in comparison to pdf_{TROP} and a much larger decrease in comparison to pdf_{IP}. Focusing on the peak of the distribution at 295 K, we note consistent changes in probabilities where higher T_b values ("clear skies") are more likely within the MJO suppressed phase in comparison to both the regional climatology and MJO active phases.

In contrast to the anticipated result that the pdf of T_b changes within the convective envelope of the MJO, Figure 3b shows the more surprising result that the tropical distribution of brightness temperature is nearly insensitive to MJO global activity. The ratio between the conditional (pdf_{OMI_A} and pdf_{OMI_I}) and climatological (pdf_{TROP}) distributions shown in Figure 3b indicate that the global tropical distribution of T_b conditioned on the presence or absence of global MJO activity is not statistically different from climatology. Note that even though there are differences along the tails, the CIs there are large because sample sizes are small in those bins. Based on the kstest described earlier, the hypothesis that both pdf_{OMI_A} and pdf_{OMI_I} are equal to pdf_{TROP} cannot be rejected at the 0.05 significance level. In this calculation, the effective sample size (N_{eff}) is estimated based on the T_b decorrelation in space and time. This decorrelation estimate is based on the mode of the zero crossings in the lag distribution, and this yields a decorrelation in space of 8° in longitude, 10° in latitude, and 33 h in time ($N_{eff} = 0.5° \times 0.5° \times 3\ h \times N/8°/10°/33\ h$). These results imply that the prominent changes in the T_b pdf within the active and suppressed MJO regions are only local and are offset by other T_b changes away

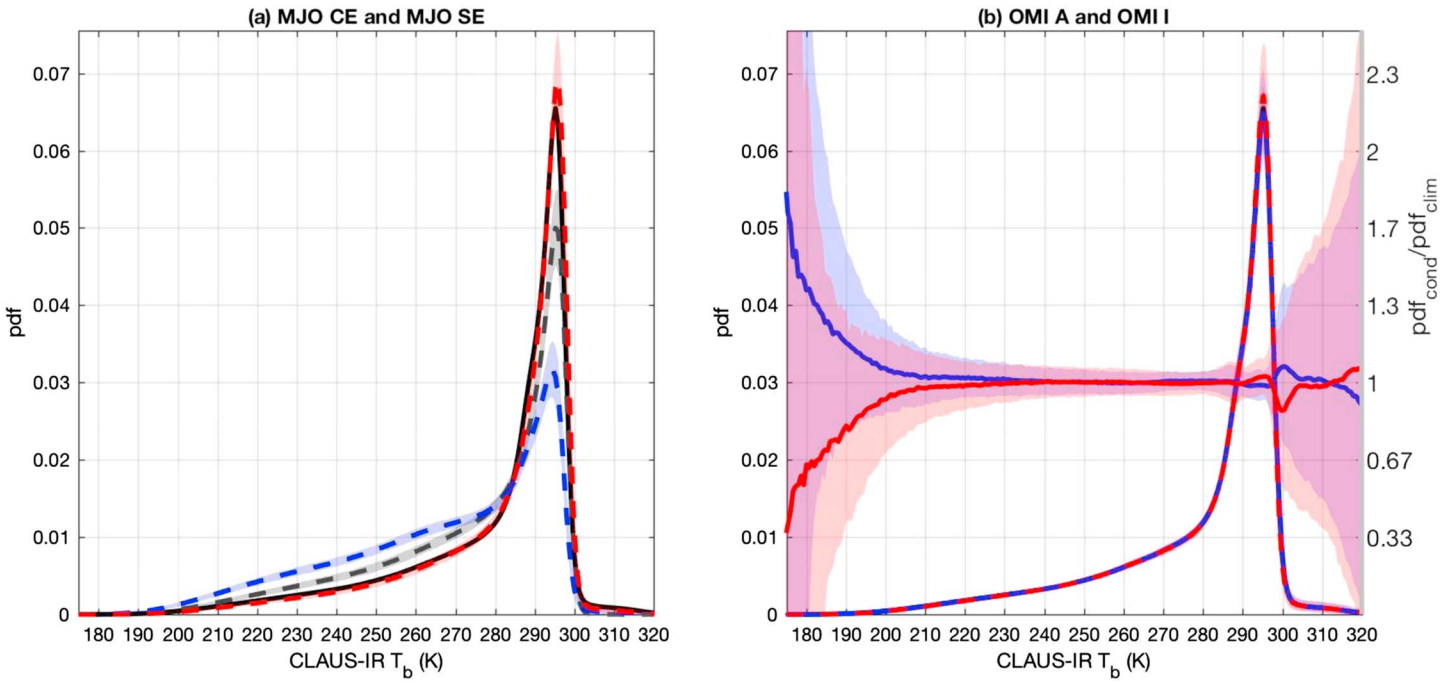

Figure 3. CLAUS-IR DJF T_b pdfs. (a) The tropical pdf (pdf_{trop}) in black, the Indo-Pacific pdf (pdf_{IP}) in dashed black, and the pdf conditioned on MJO convective (suppressed) envelopes ($pdf_{MJO_{CE}}$ and $pdf_{MJO_{SE}}$) in dashed blue (red). (b) The tropical pdf from Figure 3a overlain with the global MJO activity conditional pdfs, with red dashed standing for active MJO (pdf_{OMI_A}) and blue dashed for inactive MJO (pdf_{OMI_I}). The solid curves in Figure 3b show the ratio between the pdf conditional on OMI A and climatology (blue) and similar for OMI I (red). Shading in both panels represents the confidence interval (CI) at each bin, with colors corresponding to the pdf colors.

from the MJO convective/suppressed envelope. To verify this result, we further conditioned pdf_{OMI_A} on MJO CE and SE and then recovered the unconditional pdf by calculating a weighted average, such that

$$\begin{aligned} pdf_{OMI_A} \approx\ & n_{CE} * pdf(T_b|\text{MJO CE}|\text{OMI A}) + n_{SE} * pdf(T_b|\text{MJO SE}|\text{OMI A}) \\ & + n_{NE} * pdf(T_b|(\text{MJO CE} \bigcup \text{MJO SE})^{\perp}|\text{OMI A}) \end{aligned} \quad (1)$$

where n_{CE}, n_{SE}, and n_{NE} are the fraction of OMI A data in MJO CE, MJO SE, or neither, respectively. The left tail of pdf(T_b|MJO CE|OMI A)/pdf(T_b|MJO SE|OMI A lies above/below the left tail of $pdf_{MJO_{CE}}/pdf_{MJO_{SE}}$, and the estimated pdf is approximately equal to pdf_{OMI_A}, based on both the random sampling method and the kstest (not shown). These global insensitivities are very robust to more strict OMI activity thresholds, the examination of other seasons, and to using RMM instead of OMI to determine times of MJO strong or weak activity. In addition, the global T_b pdf (i.e., from pole to pole) and the TRMM 3B42 (50°S to 50°N) rain rate pdfs are also insensitive to MJO activity (not shown).

Interestingly, we also found evidence of the converse statement, that is, OMI amplitude does not appear to increase with the global tropical mean brightness temperature. To illustrate, Figure 4 shows the joint distribution of global tropical 15°S to 15°N CLAUS-IR T_b ($\overline{T_b}$) versus OMI amplitude for DJF. The relative flatness of this distribution indicates little dependence for OMI amplitude to be associated with colder $\overline{T_b}$. This is also confirmed by the vertical lines showing that the 15th, 50th, and 85th percentiles of OMI amplitude are nearly insensitive to $\overline{T_b}$ percentile binning. In agreement with our previous result that the distribution of T_b is insensitive to OMI amplitude, the nearly horizontal lines show that $\overline{T_b}$ is also not sensitive to OMI amplitude binning. The slight skewness of the pdf toward lower T_b values in the OMI range of 1.5 to 2 may be due to sampling issues, but this effect is very minimal and overall the shapes of the distributions are maintained throughout a wide range of OMI values.

Taken together, the results of this section imply that while the MJO tends to aggregate tropical convection spatially, it does not affect the globally integrated rainfall. More broadly, this result may be interpreted as a statement of global radiative convective equilibrium, as discussed further below.

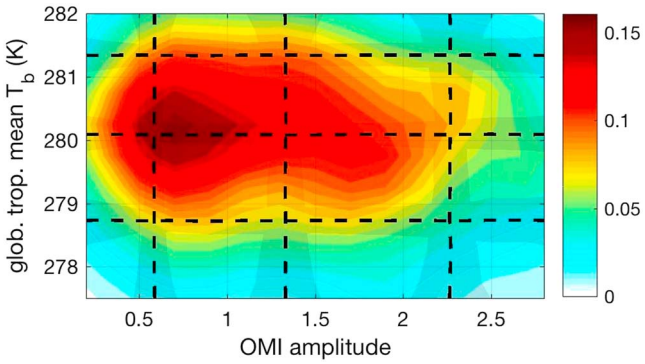

Figure 4. Color shading shows the joint probability distribution of daily global tropical mean CLAUS-IR DJF T_b ($\overline{T_b}$) and DJF OMI amplitude. The vertical black dashed lines show, from left to right, the 15th, 50th, and 85th percentiles of OMI amplitude as a function of $\overline{T_b}$. The horizontal black dashed lines are similar, except that they show, from bottom to top, the 15th, 50th, and 85th percentiles of $\overline{T_b}$ as a function of OMI amplitude. Gray shading around the dashed lines show the 95% CI of the percentile estimates.

4. The MJO and CCEW Variability

Thus far we have shown that the MJO is characterized by increased overall variance in convective activity within its envelope, even though it has minimal impact on globally convective activity. Now we would like to assess whether this variability is manifested as changes in the organization of convection. To investigate whether there is a dependence between the CCEW activity with respect to the MJO, the method described in section 2.2 is applied here to T_b filtered for individual CCEWs. These results are summarized in Figure 5 where for each filtered data set from Table 1, normalized variances within MJO CE, MJO NE, MJO SE, OMI A, and OMI are displayed for DJF. The normalization consists of dividing grid point anomalies by the DJF grid point standard deviation using the 8 times daily data. This is done so that potential MJO influences on higher-frequency variance are not unduly influenced by changes in climatological variance between the typical locations of MJO CE and SE, as might be suggested by Figure 2.

Figure 5 clearly shows that, as expected, overall CCEW variance is enhanced within MJO CE and suppressed within MJO SE in comparison to MJO NE. However, it is important to note that this is also the case for T_{bSYN}, $T_{bNOISEe}$, and $T_{bNOISEw}$ variances. The latter two are defined in Table 1 and are intentionally designed to exclude spectral peaks along Matsuno's dispersion curves [see *Kiladis et al.*, 2009]. Focusing on MJO CE/NE/SE, there are some differences in how much variance is modulated by the MJO phases. For example, WIG and NOISEe variances in MJO CE (SE) are about 30% larger (smaller) than in MJO NE; KW and EIG variances in MJO CE (SE) are about 20% larger (smaller) than in MJO NE; and ER and MRG and NOISEw variances in MJO CE (SE) are about 10% larger (smaller) than in MJO NE. From this analysis, one might conclude that WIGs are more sensitive to MJO phase. However, NOISEe is as sensitive to MJO phases as WIGs, therefore pointing to the possibility that larger modulations in variance are potentially more dependent on frequency than, for example, to the MJO large-scale environment being more favorable to WIGs over other modes of CCEWs.

While CCEW variance appears to be locally enhanced/suppressed within the MJO CE/SE, the global tropical CCEW variance is not particularly sensitive to MJO activity, as seen by hardly any change in the global activity of each mode during OMIA and OMI I, which remain close to the DJF climatology. These results suggest that, as for the global pdf of T_b shown in section 3, local enhancement/suppression of CCEW variance within MJO CE and SE average out and does not affect global CCEW variability. The conclusions for other seasons and RMM instead of OMI are very similar (not shown).

Figure 5 also brings up an important caveat of approaches based exclusively on filtering, which is that one can always apply space-time filters designed to capture particular waves to observations or model output regardless of whether convection is organized according to those modes of variability or not. This is because, by using such filtering, there is always an indeterminate amount of unrelated "background" variance that is also included within the filtering band. For example, using a variety of other metrics, *Kiladis et al.* [2016] demonstrated that convectively coupled MRG and EIG signals are primarily confined to the central Pacific region [see also *Dias and Kiladis*, 2014]. Since the bulk of the MJO CE sample region lies outside of the central

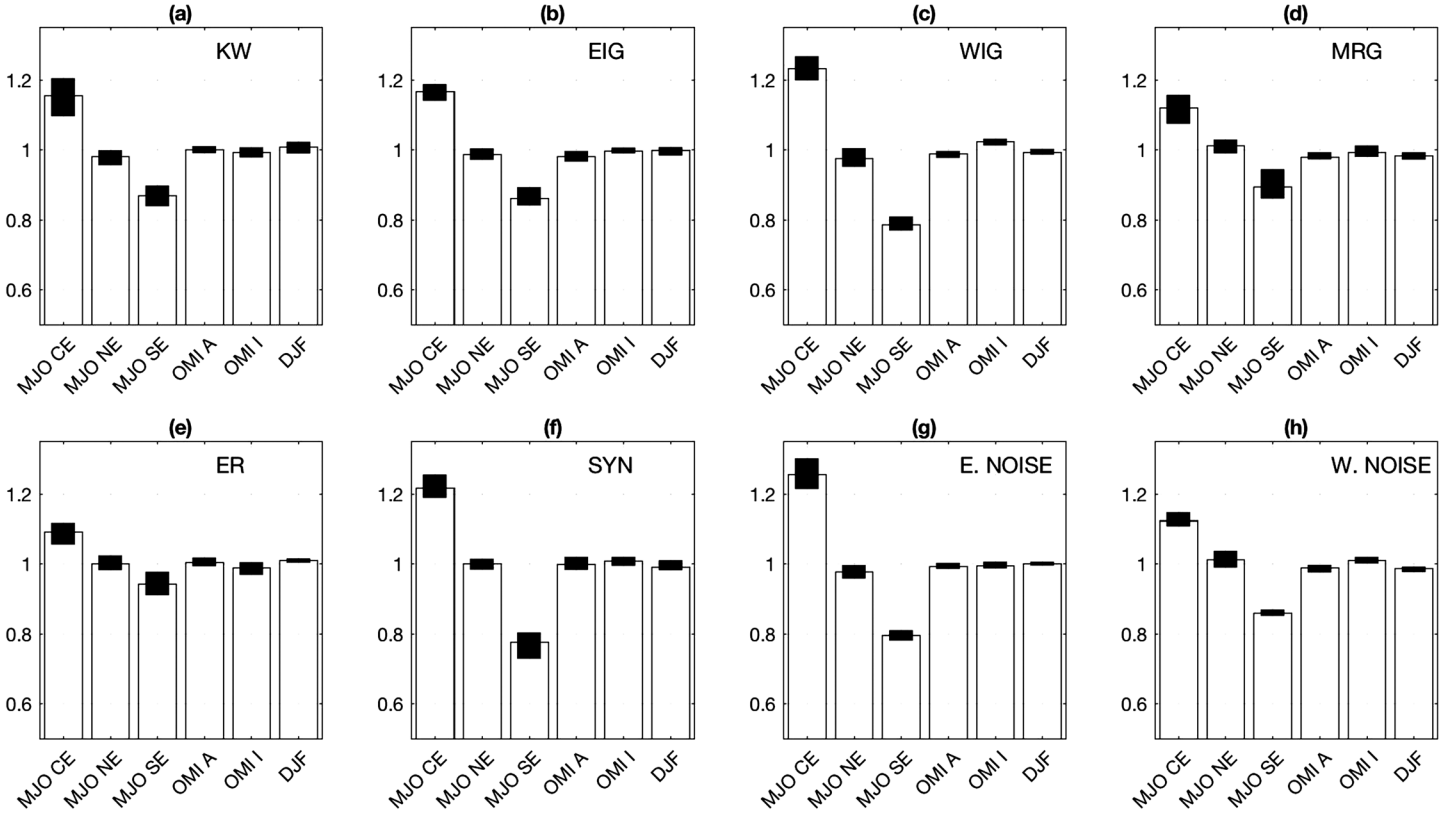

Figure 5. (a–h) Vertical bars correspond to synoptic-scale filtered CLAUS-IR T_b variance normalized to the DJF climatology, which has a value of 1. From left to right, for MJO CE, MJO NE, MJO SE, OMI A, OMI I, and DJF. Black rectangles show the confidence intervals for the variance estimates (see details in the text). Each panel corresponds to a filtering band from Table 1, and their labels are displayed on the upper right corner of each panel.

Pacific (Figure 2), this strongly suggests that the local variance enhancements of these waves within the MJO convective envelope shown in Figure 5 may be due simply to an overall local enhancement in background convective variability that is not related to those particular modes. We note that the methodology used in *Dias et al.* [2012] was aimed at circumventing this type of filtering issue, and it provides a more detailed view of how the MJO, locally, does not favor any particular mode of CCEW.

Keeping in mind issues regarding background noise, to further investigate whether modulations of CCEW variance by the MJO are systematic in any other way, Figure 6 displays histograms representing normalized CCEW variance for individual MJO CEs. To obtain these distributions, MJO events are selected as in Figure1 by considering each enclosed blue line as one MJO event. Using the entire record, we select all enclosed contours that occur during DJF. The centroids are defined as the T_{bMJO} weighted centroid coordinates in the longitude-latitude time-space of each enclosed region. The large spread in normalized CCEW variance from one event to another in Figure 6 is clear for all modes, demonstrating that while the mean variance shown in Figure 5 is near the median variance (red symbols in Figure 6), they are not particularly representative of any individual MJO event. Moreover, there are similarly large spreads in the normalized variance for T_{bSYN}, $T_{bNOISEe}$, and $T_{bNOISEw}$. The event-by-event correlations between unfiltered T_b variance and filtered T_b variances within MJO convective envelopes (Table 2) are generally positive, suggesting that once again, to some extent, the variance within each CCEW spectral region is enhanced when overall T_b variance is enhanced. In addition, the fact that these correlation values vary mode by mode and that they are not especially large demonstrates that the synoptic make up of the MJO is very diverse on an event-by-event basis. Taken together, these variance correlations across modes further supports the notion that convective variability is enhanced at most space-time scales within the MJO convective envelope, and that this enhancement does not necessarily imply more intense organization along any specific CCEWs dispersion curves.

To demonstrate how the contamination from background noise can lead to conflicting results, we use our case-by-case approach to further investigate the relationship between MJO amplitude and CCEW activity.

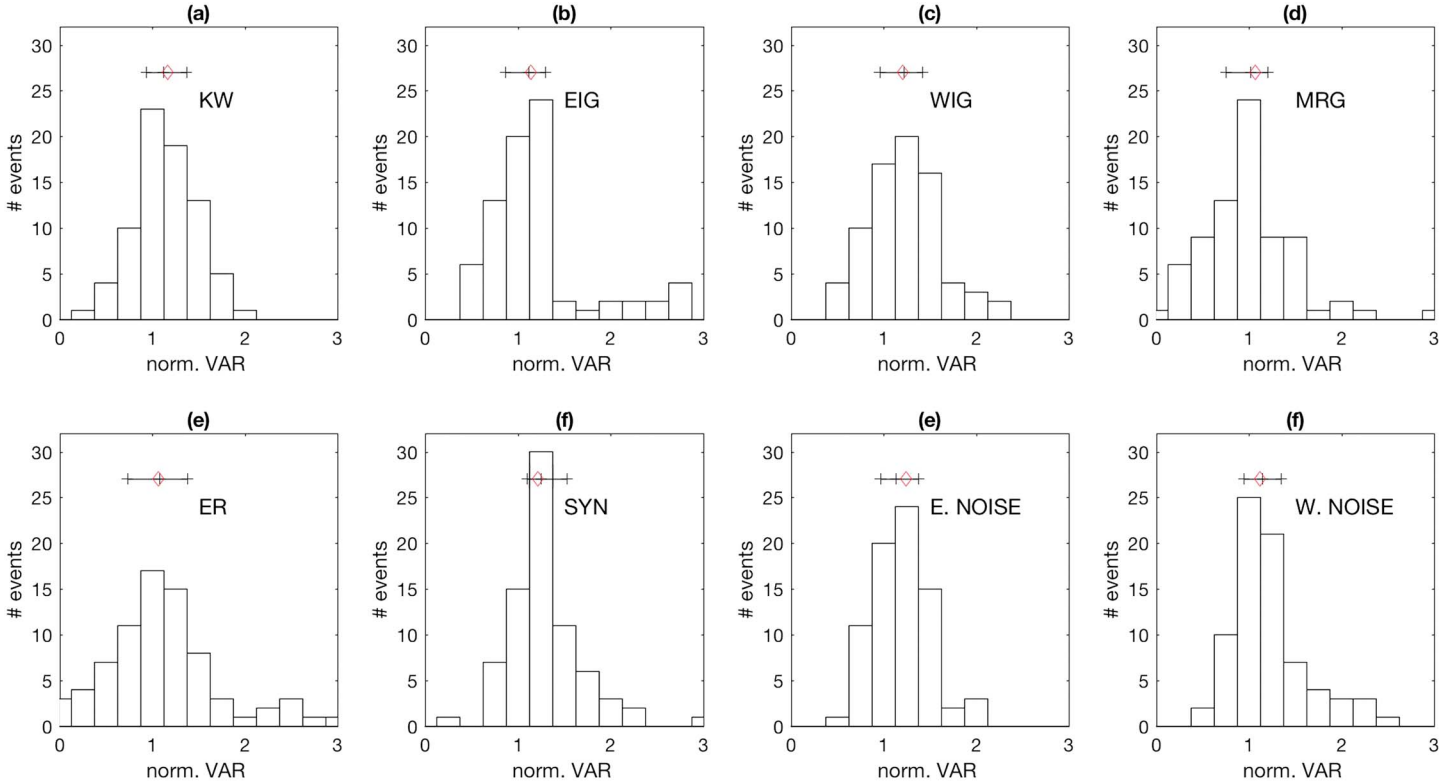

Figure 6. Histograms of DJF CLAUS-IR T_b normalized variance for MJO convective events (defined in the text). Each panel correspond to a filtering band from Table 1 and their labels are displayed on the upper right corner of each panel. Lower, middle, and upper quartiles are shown as a black line in each panel. The red symbol corresponds to the normalized variance from Figure 5.

This relationship is a key ingredient of the"Skeleton" MJO theory [*Majda and Stechmann*, 2009, 2011; *Stechmann and Majda*, 2015], in which the amplitude of the synoptic wave activity envelope interacting with planetary-scale lower tropospheric moisture anomalies is a major factor determining the strength of the MJO. In addition, *Guo et al.* [2015] suggest that models with stronger synoptic convective activity tend to have a better representation of the MJO. Assuming that CCEW variance is a proxy for overall wave activity amplitude, one would expect a positive correlation between MJO amplitude and CCEW amplitude as was seen, for example, in Figure 5f. To investigate this issue from an event-by-event point to view, a scatterplot of T_{bSYN} normalized variance within each MJO CE versus MJO amplitude is shown in Figure 7, where the MJO amplitude is defined here as the minimum of T_{bMJO} for each individual MJO CE event. Figure 7 shows that the relationship between strength of T_b synoptic variance and MJO amplitude is not well defined. For instance, while strong MJO events

Table 2. Correlations Between Raw and Filtered T_b Normalized Variance Within MJO Convective Envelopes Calculated Event by Event (Same Events as Shown in Figure 6)[a]

	T_b	KW	EIG	WIG	MRG	ER	SYN	NOISEe	NOISEw
T_b	1.0	0.11	NS	NS	0.33	0.12	0.12	NS	0.27
KW		1.0	0.28	0.21	0.40	NS	0.25	0.34	NS
EIG			1.0	0.41	0.14	NS	0.16	0.18	−0.12
WIG				1.0	0.16	0.22	0.47	0.42	0.11
MRG					1.0	NS	0.25	0.24	0.13
ER						1.0	0.44	0.26	0.18
SYN							1.0	0.27	0.28
NOISEe								1.0	0.38
NOISEw									1.0

[a]The correlations that are not significant are labeled "NS".

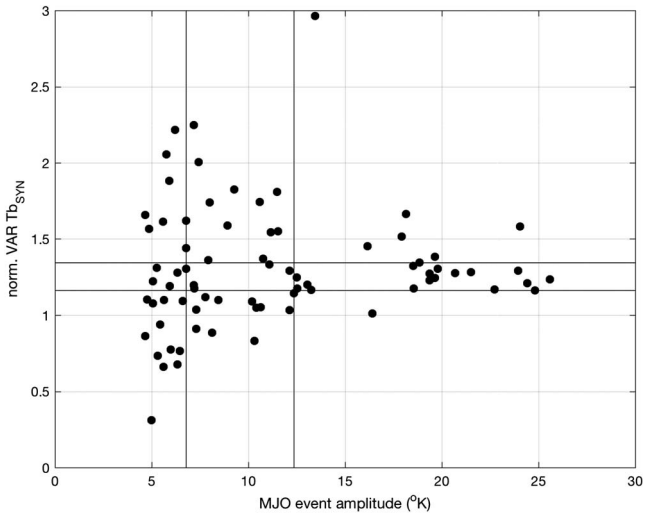

Figure 7. Scatterplot of MJO suppressed envelope amplitude and normalized T_{bSYN} variance. The horizontal and vertical lines correspond to the terciles of the two variables.

are about evenly partitioned between moderate and strong synoptic variance, weak MJO events have the largest spread in synoptic variance. In fact, the cases with largest synoptic variance are associated with relatively weak MJO amplitudes. Other scatterplots, except for individual CCEW modes or more strict definitions of MJO CE and SE, display very similar patterns (not shown). Therefore, based on the metrics used here, we conclude that while overall CCEW variance is enhanced within active MJOs compared to climatology, there is no clear relationship between the amplitude of the MJO and the level of synoptic wave activity within it.

Since there is no consensus on how to remove background variability from filtered data, it is difficult to access what fraction of the statistical relationships shown in Figures 4 and 5 is due to an overall enhancement in convective variability versus some physical mechanism relating synoptic and low-frequency variability. The fact that our analysis suggests that the amplitude of individual MJO cases is not clearly related to synoptic variability embedded in its planetary-scale convective envelope is an indication that increases in CCEW variance within the MJO convective phase are primarily due to the enhancement of the background.

5. Tropical Mesoscale Convective Organization

We now extend our analysis to the relationship between the MJO and tropical mesoscale convective organization. Mesoscale features of tropical T_b are defined as contiguous regions in longitude×latitude×time-space, where T_b is below a particular threshold. The detection algorithm is summarized in the next subsection and is described in further detail in *Dias et al.* [2012]. As in *Dias et al.* [2012], objects in the T_b data set are denoted CCRs, which stands for "contiguous cloudy regions." Following the approach from previous sections, CCRs are tagged depending on whether their T_b weighted centroids fall into the MJO CE, MJO SE, OMI A, or OMI I categories. CCR conditional statistics (e.g., lifetime and size) are then compared to climatology.

5.1. Review of the Object-Tracking Approach to Assess Convective Organization

The first step in detecting CCRs is to choose a T_b threshold (T_b^0). Based on the results of *Dias et al.* [2012] T_b ranges from approximately 230 K to 245 K (5th to 10th percentiles of T_b from 15°S to 15°N) yield the largest spread in some key characteristics of CCRs (see their Figure 5), and the number of CCRs maximizes at the 5th percentile (see their Figure 4a). In the present manuscript, we focus on the 230 K threshold and sensitivities are noted when necessary. As in *Dias et al.* [2012], the CCR properties that we analyze are lifetime, width, and phase speed. Lifetime is defined as the latest minus the earliest time when the CCR is detected. CCRs are three-dimensional in the space of longitude, latitude, and time. To calculate zonal width and zonal phase speed, the three-dimensional CCRs are first averaged in latitude and then zonal width is estimated in the CCR longitude-time domain and defined as the mean zonal extension over the CCR lifetime. The phase speed is determined using a best fit method based on a radon transformation, which is also applied to the meridionally averaged CCR, and when the best fit method does not converge, the CCR is tagged as "nonpropagating." Determination of the meridional width and phase speed is analogous, except that CCRs are averaged in the

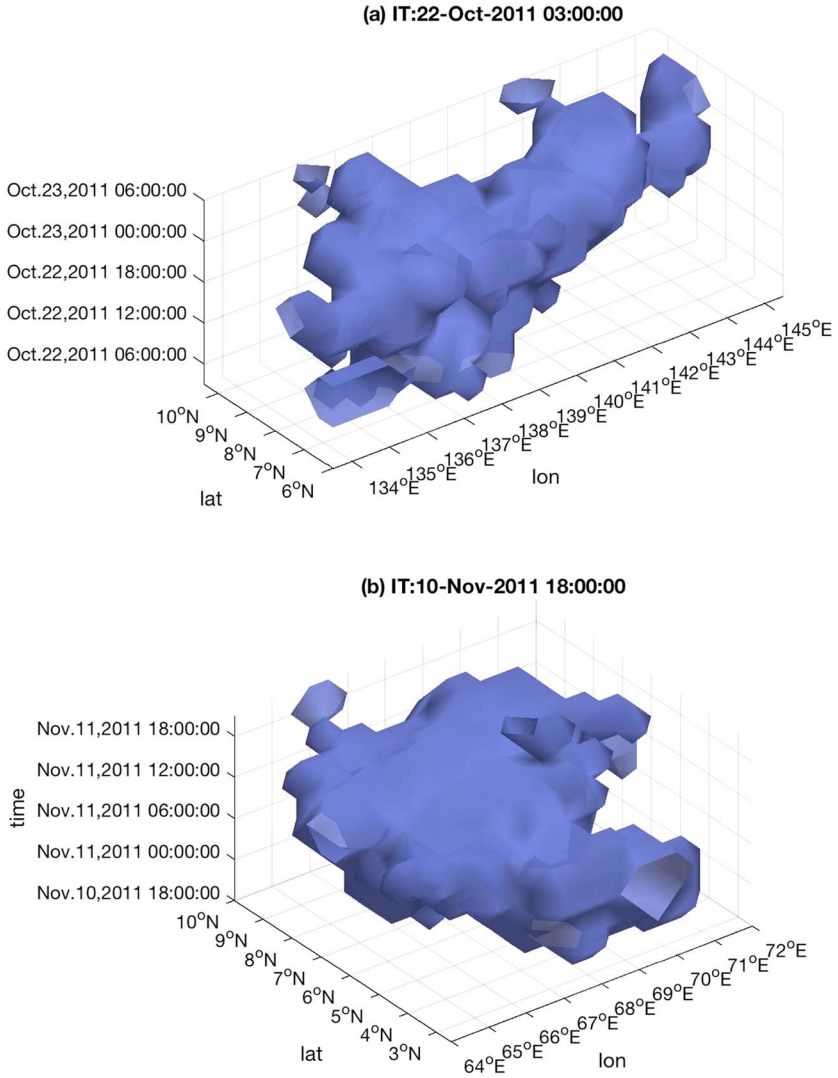

Figure 8. (a and b) Examples of CLAUS-IR DJF CCRs for a threshold $T_b = 230$ K. Shading represents the boundaries of each CCR in latitude-longitude time-space. The initial time (IT) for each panel is displayed in the title.

zonal direction. The main difference between the CCR data set used here and that in *Dias et al.* [2012] is that here we chose to include smaller-scale CCRs. Specifically, we retain all CCRs that last more than 9 h and span at least 200 km in longitude or latitude. The CCR data set is also extended to 31 December 2013 using the calibrated IR data. As a test of the calibration method, the statistics of CCRs were calculated separately using the CLAUS data and the calibrated IR data, and these are virtually identical.

As an illustration, two examples of CCRs are shown in Figure 8. The first example initiated on 22 October 2011 off the east coast of the Philippines and moved primarily toward the east for about a day. The second example initiated on 10 November 2011 to the west of the Maldives and also lasted for about a day; however, its zonal propagation was not as clear. Based on speed estimates, the eastward and northward speeds in Figure 8a are 15 ms^{-1} and 2.5 ms^{-1}, whereas in Figure 8b the zonal speed is not defined and the northward speed is 18 ms^{-1}. Table 3 shows that there are over 30,000 CCRs that meet our selection criteria, where about 45% of them fall in MJO CE or in MJO SE, and about 30% in MJO A or in MJO I.

Table 3. Total Number of Identified CLAUS T_b DJF CCRs

Subset:	Clim.	MJO CE	MJO SE	OMI A	OMI I
# CCRs:	30482	7025	6880	5623	4726

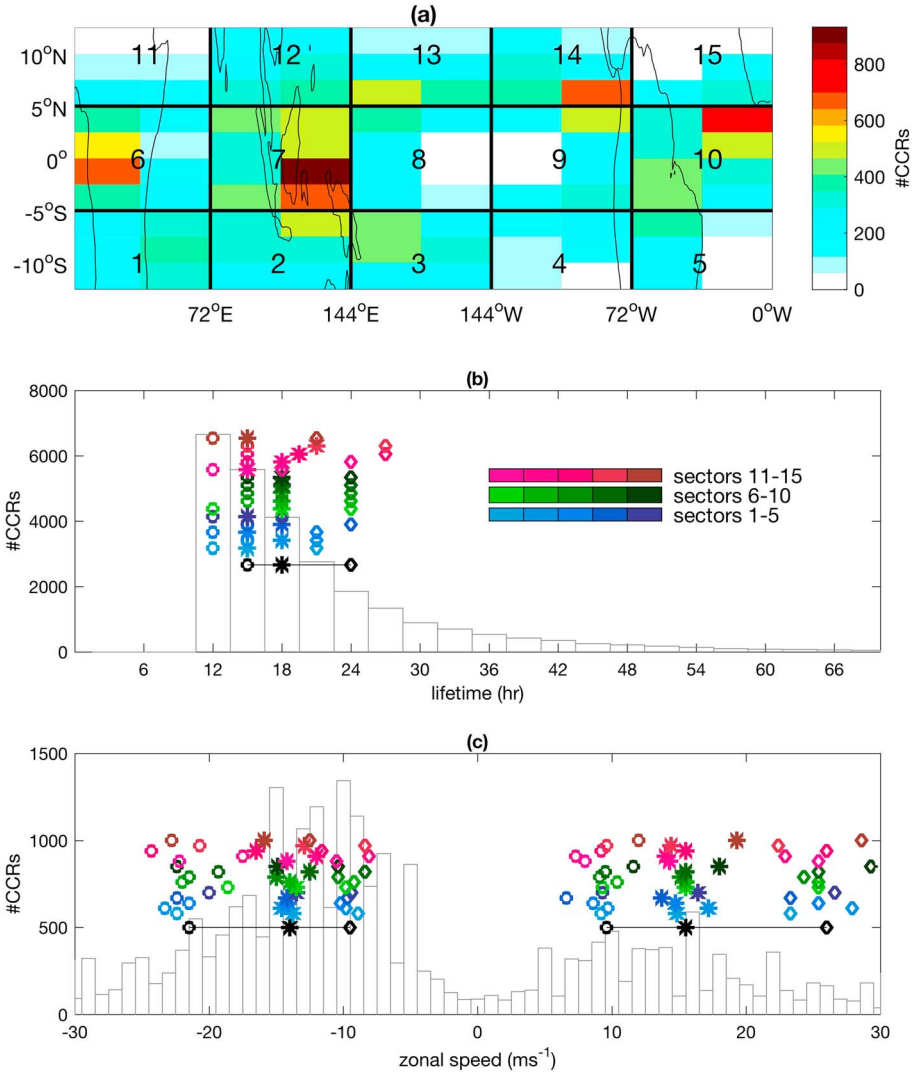

Figure 9. Histograms of CLAUS-IR DJF CCRs for a threshold $T_b = 230$ K. (a) The number of CCRs by latitude-longitude bins (CCR coordinates are based on their centroids). (b) Gray bars display the histograms of CCR lifetime for the global climatology and for the three sectors shown in Figure 9a. (c) Similar to Figure 9b except for zonal phase speed. In Figures 9b and 9c, black symbols correspond to lower (circle), middle (asterisk), and upper (diamond) quartiles of the same distributions. The colored symbols are similar but for quartiles within each sector defined in Figure 9a. Each color corresponds to one sector, and the color table is shown in Figure 9b.

Regarding the geographical distribution of CCRs, it is important to note that local T_b pdfs vary substantially in comparison to pdf_{TROP} shown in Figure 3. For example, while 230 K represents the 5th percentile of pdf_{TROP}, it corresponds to the 25th percentile of certain regions such as the Maritime Continent. As a consequence, there are strong biases in locations of CCRs as it is illustrated by the latitude-longitude histogram of CCR centroids shown in Figure 9a. For instance, Figure 9a shows that the total number of CCRs is closely tied to the local frequency of $T_b < 230$ K, with a global peak over the Maritime Continent and secondary peaks over the eastern Pacific and Africa. In contrast to the geographic localization of CCR occurrence, one remarkable feature of CCRs is that their main properties are surprisingly invariant throughout the tropics. This is illustrated by Figures 9b and 9c, which show the tropical DJF histograms of lifetime and zonal speeds, overlaid with histograms for the zonal sectors highlighted in Figure 9a. The most common lifetime for tropical CCRs is 12 h, and the median lifetime is 18 h. CCR lifetime is fairly uniform across tropical regions. Figure 9c shows that in all sectors most CCRs propagate to the west, which is consistent with the mesoscale to synoptic-scale westward bias in the global space-time spectra of T_b [see *Tulich and Kiladis*, 2012]. In addition, most CCRs propagate between 9 and 20 ms^{-1} in both eastward and westward directions. Other quantities such as meridional speed and widths

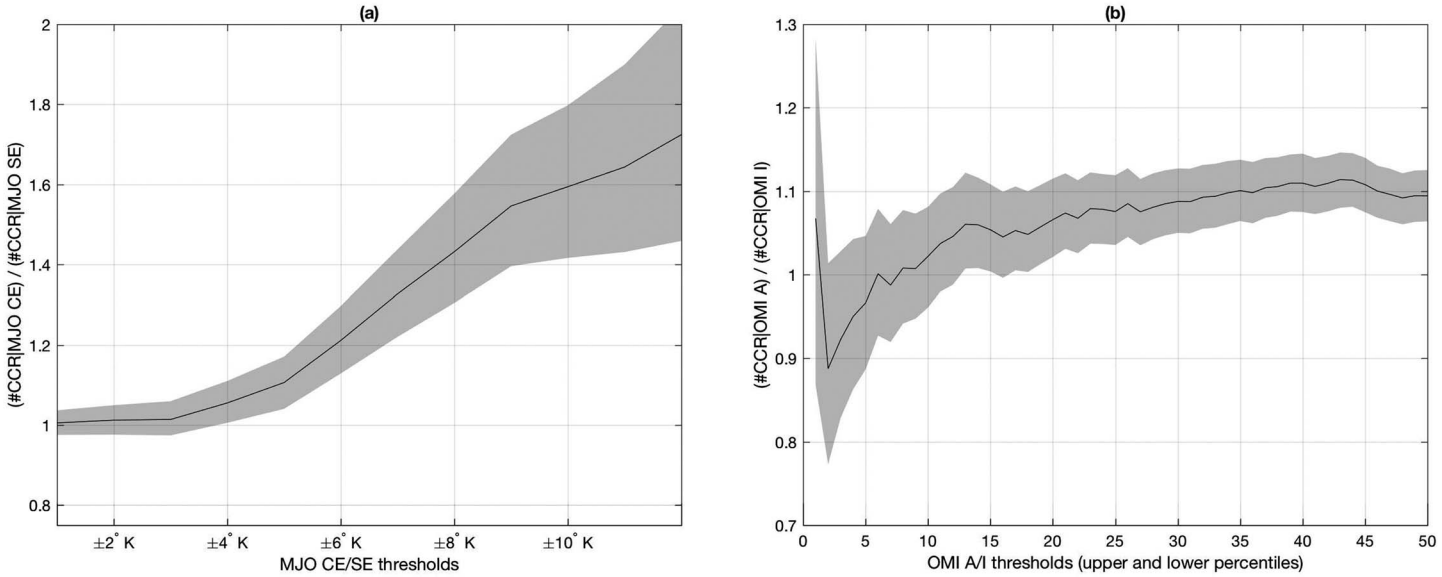

Figure 10. (a) Ratio of CCRs in MJO CE versus MJO SE as a function of MJO envelope threshold. (b) Similar to Figure 10a except for OMI A versus OMI I. Shading represents the bootstrap 95% confidence interval (CI) at each threshold.

are also similar across regions (not shown). Following the approach from the previous sections, we analyze CCRs depending on whether they fall in MJO CE or SE, and similarly, whether they fall in OMI A or OMI I. We assume a CCR belongs to MJO CE if its T_b weighted centroid grid point falls inside a MJO CE. Similar definitions were used for MJO SE and for OMIA A and OMI I. We tested alternatives such as requiring that half of each CCR grid points belong to a MJO CE in order for it to be identified as a CCR in MJO CE, but our main conclusions remained the same over a wide variety of criteria.

Based on the tropical T_b pdf analysis, which shows a higher (lower) probability of low T_b values in MJO CE (SE), modulation could potentially impact CCRs in MJO CE versus MJO SE in two different ways, perhaps in combination. The first one is that the frequency of CCRs might increase in MJO CE in comparison to MJO SE, but that their sizes would be comparable. The second possibility is that there would be fewer CCRs in MJO CE, but they would tend to be larger than in MJO SE. Figure 10a shows that for all thresholds exceeding ±4K, which defines MJO CE and MJO SE regions, there are always more CCRs in MJO CE than in MJO SE. To investigate if there are changes in CCR sizes in addition to the change in frequency of occurrence, Figures 11a, 11c, 11e, and 11g show the climatological histograms of some CCR characteristics, as well as their conditional histograms for MJO CE and SE. Simply stated, apart from the change in frequency of occurrence, there is no systematic difference in any of the CCR characteristics conditioned on MJO CE, MJO SE, or OMI A and OMI I. The fact that CCR life spans and widths are not sensitive to whether they develop within the MJO CE or SE, in addition to the increase in the ratio of CCRs in MJO CE to MJO SE, indicates that CCR sizes are comparable to climatology in both phases of the MJO, but there are relatively more of them in MJO CE. Furthermore, Figure 11e through Figure 11h suggest that CCR zonal and meridional propagation speeds are also not sensitive to MJO phases. The kstest between climatology and MJO subsamples is in agreement with the random sample significance test, except for the zonal speed in MJO SE in comparison to climatology. According to the kstest, the small increase (decrease) in probability of eastward (westward) CCRs in MJO SE (shown in red in Figure 11e) is significant. We have also tested varying bin sizes, and we still find that the bin CIs overlap, perhaps due to the limited sample sizes. In other words, it is possible that with a larger sample of CCRs, differences such as the larger fraction of CCRs in MJO SE that are short lived (<18 h, shown in red in Figure 11e) would become significant. However, our results seem to imply that there are no substantial changes in CCR characteristics within the MJO convective or suppressed phases.

In a global sense, because the OMI A and OMI I T_b conditional pdfs are the same as climatology, any changes in CCR morphology would have to be compensated by a change in number of CCRs. In contrast, Figure 10b shows that there are more CCRs in OMI A than in OMI I for thresholds beyond the upper and lower 12th DJF OMI percentiles, and that this ratio does not converge to 1 for percentiles approaching the median.

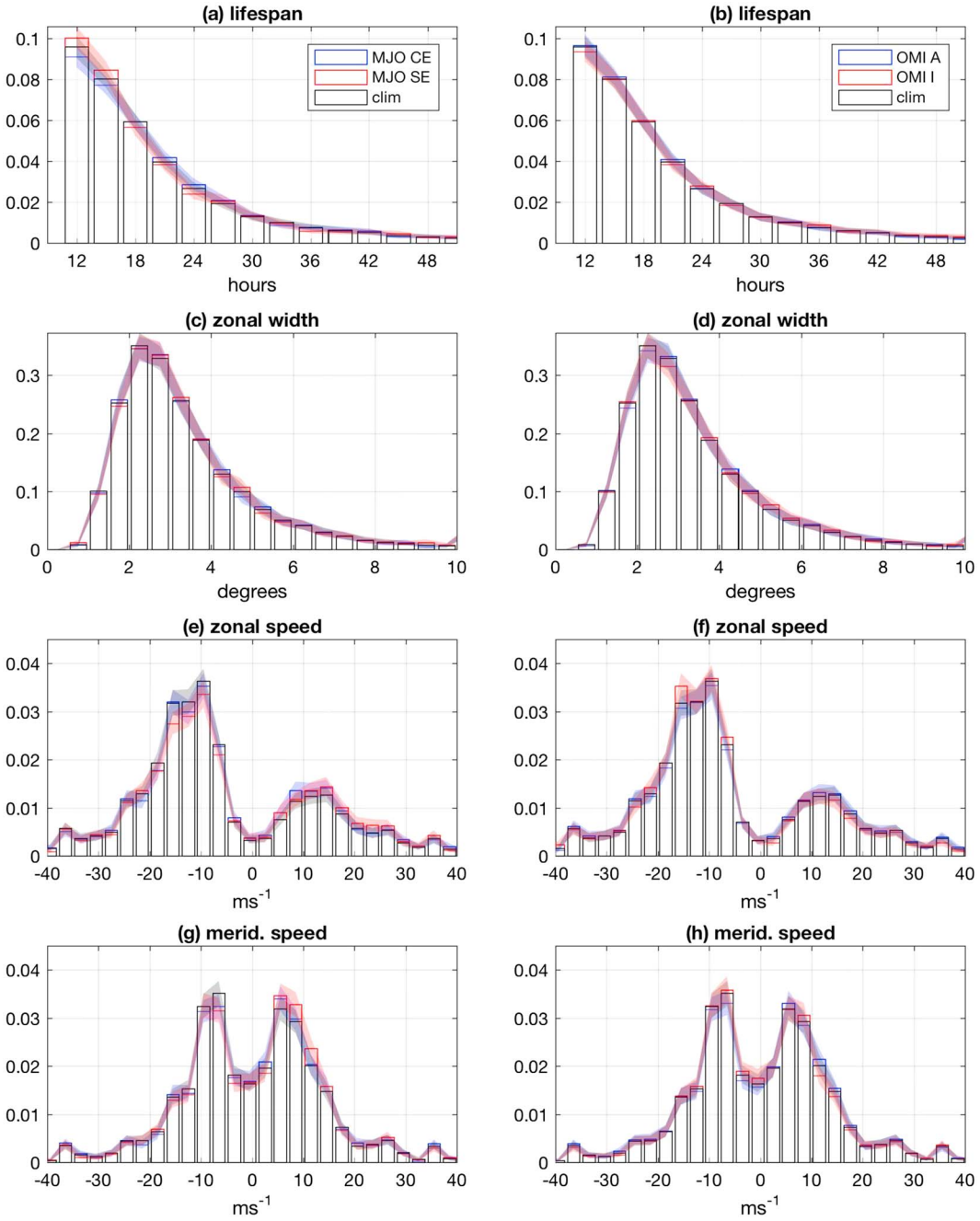

Figure 11. Summary of DJF CLAUS-IR T_b CCR pdfs. In all panels black bars correspond to normalized climatological histograms. (a, c, e, g) Blue (red) bars correspond to normalized histograms conditional on MJO CE (SE). (b, d, f, h) Blue (red) bars are similar except conditioned on OMI A (OMI I). Figures 11a and 11b show lifetime; Figures 11c and 11d show zonal width, Figures 11e and 11f show zonal propagation speed, and Figures 11g and 11h show meridional propagation speed. Shading corresponds to the confidence interval (CI) in each bin using colors consistent with the histograms.

While this seems to imply that CCRs should be either wider or last longer in OMI A, Figures 11b, 11d, 11f, and 11h nevertheless show no statistical difference between CCRs during active or inactive MJO periods (results that are confirmed by the kstest). It turns out that this apparent discrepancy is a result of the combined impact of the seasonal cycles of OMI and T_b. During DJF, OMI activity is lowest in December, which is also the month with fewest CCRs. As a result the ratio shown in Figure10b is below 1 during December but above 1 in January and February. Because there are more CCRs in January and February the net result is a ratio slightly larger

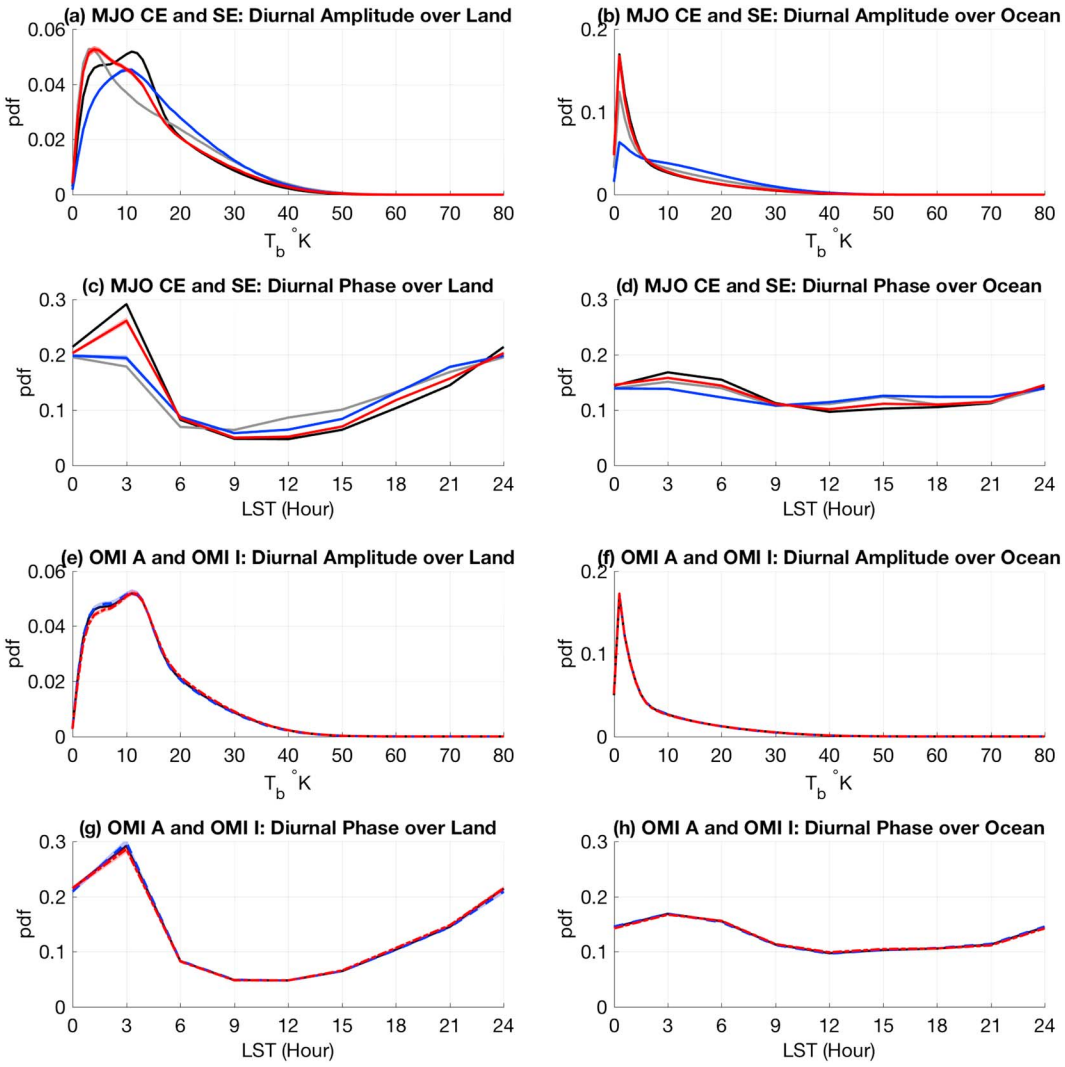

Figure 12. The DJF CLAUS-IR T_b (a and b) diurnal cycle amplitude and (c and d) diurnal cycle phase where black is the tropical pdf, gray is the Indo-Pacific pdf, red is the MJO SE, and blue is the MJO CE conditional pdfs. DJF CLAUS-IR T_b (e and f) diurnal cycle amplitude and (g and h) diurnal cycle phase where black is the tropical pdf, red is the for OMI I, and blue is for OMI A. Figures 12a, 12c, 12e, and 12g show the pdfs over land, and Figures 12b, 12d, 12f, and 12h show the pdfs over the ocean.

than 1. We have tested our results by calculating monthly OMI thresholds, which confirms the overall lack of changes in both CCR frequency and morphology with respect to the OMI (not shown).

6. The Diurnal Cycle of Tropical Convection

In this section we calculate conditional pdfs of the amplitude and phase of the diurnal cycle of tropical convection inferred from CLAUS-IR T_b, using the methodology of *Sakaeda et al.* [2017]. Briefly, the amplitude and phase of the diurnal cycle of 3-hourly T_b are estimated using harmonic analysis for each grid point and day in the entire data set. The statistics of the diurnal cycle are then conditioned on MJO characteristics as in previous sections. Consistent with past studies [e.g., *Yang and Slingo*, 2001; *Kikuchi and Wang*, 2008], most of the amplitude of the total intradiurnal variability is explained by the first harmonic of diurnal cycle during DJF, being 63% of the variance on average over the global tropics. The phase of the diurnal cycle presented here is represented by the local solar time when the T_b amplitude reaches its diurnal minimum or near the time when convective clouds peak. It turns out that the diurnal cycle of T_b does not necessarily match the diurnal cycle of rainfall because T_b represents the diurnal cycle of both precipitating and nonprecipitating clouds, along with surface temperatures over clear regions [*Sakaeda et al.*, 2017]. Some previous studies excluded days with T_b

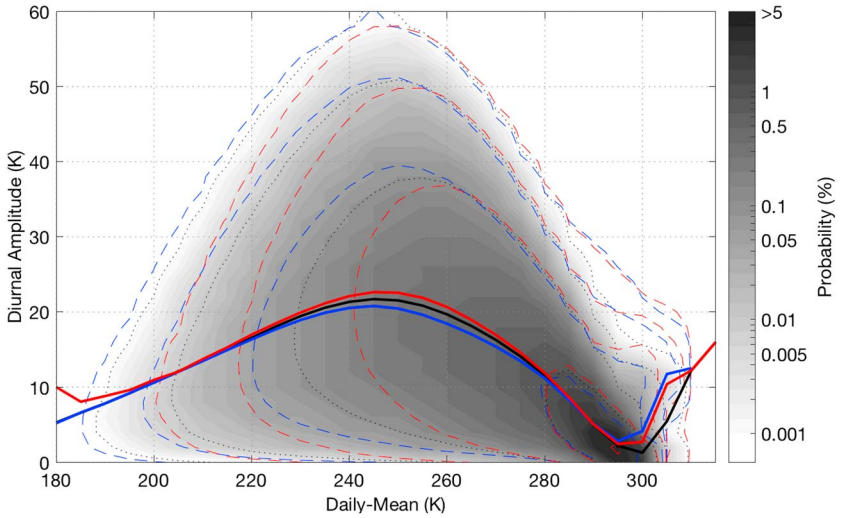

Figure 13. Joint pdf of DJF CLAUS-IR T_b daily mean and diurnal amplitude (shading) for the Indo-Pacific region. The black dotted lines show the contours at 0.001%, 0.01%, 0.1%, and 1% probabilities. The dashed blue and red contours are similar except for the conditional joint pdf of MJO CE and MJO SE. The solid lines are the weighted mean diurnal amplitude for each daily mean T_b bin, where colors correspond to climatology (black), MJO CE (blue), and MJO SE (red).

above some threshold value, in order to eliminate the inclusion of diurnal cycle from clear-sky surfaces [e.g., *Chen and Houze*, 1997; *Yang and Slingo*, 2001; *Suzuki*, 2009]. As shown below, results are quite sensitive to threshold values [e.g., *Albright et al.*, 1985; *Chen and Houze*, 1997] so all days and points are included without any threshold elimination.

Normalized pdfs of diurnal cycle statistics of T_b conditioned on the MJO following the same definitions (MJO CE, MJO SE, etc.) as in the previous sections are shown in Figure 12. The sharp peak in diurnal amplitude at around 1 K in Figures 12b and 12f comes from the diurnal cycle of clear-sky sea surface temperature (not shown). Overall, Figures 12a and 12b show results consistent with the analysis of TRMM precipitation by *Sakaeda et al.* [2017], in that the probability of a large diurnal amplitude of T_b is higher in MJO CE in comparison to MJO SE, as well as in comparison to the global tropical probabilities over both land and ocean.

The relative larger T_b diurnal amplitude within MJO CE is not too surprising, since this was also found to be the case for diurnal rainfall amplitudes using TRMM 3B42 by *Sakaeda et al.* [2017]. In that case it was found that while the diurnal cycle amplitude increases from suppressed to enhanced MJO convection, its ratio to daily mean precipitation decreases. In other words, even though the diurnal rainfall amplitude becomes greater, its relative contribution to total rainfall variance within the MJO envelope becomes smaller. The analogous statement is more complicated when dealing with T_b because, as mentioned above, the T_b diurnal cycle represents both precipitating and nonprecipitating clouds along with clear-sky conditions. In contrast to the strong positive correlation between daily mean rainfall rate and its diurnal amplitude, the relationship between T_b daily mean and diurnal amplitude is far from linear, as demonstrated by their joint pdf (Figure 13). The black curve in Figure 13 shows the statistical relationship between T_b daily mean and diurnal amplitude based on the frequency weighted daily amplitude for each daily mean bin. This curve indicates that the diurnal amplitude of *Tb* tends to increase with increasing daily mean T_b for less than about 245 K, whereas it has the opposite relationship for T_b larger than about 245 K. In combination with the much higher probability of occurrence of 300 K> T_b > 245 K than T_b < 245 K (shading), the slope of the black curve in this range suggests that the diurnal cycle amplitude is likely to be larger for smaller T_b daily mean values. However, the ratio between diurnal amplitude to the daily mean tends to be larger in MJO SE (red curve) than in MJO CE (blue curve). That is, the increase in diurnal cycle amplitude from MJO SE to MJO CE is smaller than the decrease in the daily mean T_b from MJO SE to MJO CE. These features are consistent with TRMM 3B42 precipitation results of *Sakaeda et al.* [2017].

The distribution of the diurnal phase also varies between MJO CE and SE. The flatter distribution of the diurnal phase within MJO CE (Figures 12c and 12d) indicates that the timing of diurnal cloudiness peaks within MJO CE is more uniformly distributed than within MJO SE, which shows a more pronounced peak in the early morning.

The early morning peak over ocean is partially due to the diurnal phase of rainfall being more pronounced in MJO SE than in MJO CE [see *Sakaeda et al.*, 2017, Figure 9b], but it also includes the clear-sky surface diurnal cycle. The inclusion of the clear-sky surface diurnal cycle makes the interpretation of the diurnal phase pdf difficult. The reasons for changes in the diurnal phase in MJO SE and CE are further discussed using TRMM rainfall data in *Sakaeda et al.* [2017].

Once more, as in the global distribution of T_b conditioned on the MJO in Figure 3, Figures 12e–12h show that there are no changes in the global tropical pdfs of diurnal amplitude or phase associated with the presence or absence of an active MJO. Therefore, as with CCEW variance, the local MJO modulations of diurnal amplitude and phase balance in such a way that their global distributions are not altered. In contrast to the global MJO activity, the local modulations of the diurnal phase and amplitude by the MJO (i.e., in MJO CE/MJO SE) differ over land and ocean in complex ways, and we refer to *Sakaeda et al.* [2017] for a more detailed analysis of these relationships.

7. Summary and Conclusions

In this study, a variety of diagnostics are applied to CLAUS-IR (T_b) data in order to investigate the relationship between the MJO and higher frequency organized tropical convection. To distinguish between local and global effects, we follow a standard approach of applying a space-time filter to CLAUS-IR T_b, which allows us to decompose the data into negative and positive MJO anomalies, representing convective (MJO CE) and suppressed (MJO SE) regions. For a global index of MJO activity, we use the OMI, which is an OLR-based MJO index, and we compare times when the index is high versus low amplitude, indicating active (OMI A) or inactive (OMI I) MJOs. Local and global statistics of CLAUS-IR T_b pdfs, CCEW variance, mesoscale (MCS) organization, and the diurnal cycle are investigated with respect to these MJO indices. Although we do not show results for more direct measures of tropical rainfall, we have verified that our overall conclusions do not change when using TRMM 3B42 data, except for the slight shift in the phase of the diurnal cycle discussed above and in *Sakaeda et al.* [2017].

The CLAUS-IR T_b pdf conditional analysis shows that in comparison to the global tropical climatology, low T_b values are more (less) likely to occur within the MJO convective (suppressed) phase. However, periods of intense and weak MJO activity are, on average, not associated with changes in the globally integrated CLAUS-IR T_b. Taken together, these results suggest that the MJO acts to redistribute convection spatially, but that it does not affect the integrated global tropical convective activity. From the standpoint of satellite irradiance measurements of T_b, this might imply that there is a global constraint due to radiative convective equilibrium, although similar results are obtained using TRMM 3B42 rainfall estimates. These results are also valid over the entire globe from pole to pole when using T_b and also from 49°S to 49°N when using TRMM 3B42 rainfall. Based on this result, one might speculate that improving MJO variability in a numerical model should also improve the spatial distribution of the tropical rainfall mean state, without necessarily affecting the total tropical precipitation. In contrast, a number modeling studies [*Kim et al.*, 2011, 2012; *Benedict et al.*, 2013] have shown that parameter changes that improve the MJO tend to worsen general circulation models (GCM) mean state biases, including increased total precipitation. The results shown here suggest an observational constraint to models, whereby model developments aimed at improving MJO variability should not impact total amounts of tropical rainfall.

This local change in the MJO conditional pdf (Figure 3) implies that T_b variance is larger in MJO CE than in MJO SE. By filtering CLAUS-IR T_b for various CCEW spectral regions, we find that the variance associated with all modes studied increases within the MJO active phase and decreases within the MJO suppressed phase; however, in an event-by-event analysis, we show that there is a large spread in the overall strength and distribution of CCEW activity across individual MJO events. This is an important point because it suggests that the increase (decrease) in CCEW variance may simply occur because of an overall increase (decrease) in background T_b variance, and not because CCEWs become more organized (disorganized) within the MJO CE (SE). Our global analysis using OMI shows that the integrated tropical variance of CCEWs are not sensitive to MJO activity. An implication for model development is that verification metrics based purely on diagnostics of the variance of CCEWs [e.g., *Guo et al.*, 2015] might not be wholly representative because they do not imply that tropical variability necessarily becomes more organized following Matsuno's dispersion curves, but rather that background *Tb* variance is enhanced.

We note that because broad spectral regions are used to define CCEW modes, we cannot address the question of whether the MJO affects, for example, Kelvin wave propagation speeds as it has been suggested in other studies [*Roundy*, 2008; *Dias et al.*, 2013]. Our findings do not contradict MJO-related modulation of CCEW propagation speeds because these changes in dispersion characteristics are small enough that most of the variance associated with the potentially slower modes is still accounted for when using our choices of filtering regions. Our results simply imply that, for example, any increase in variance associated with slower Kevin waves within MJO CE is not particular to this mode of variability. *Yasunaga* [2011] also investigated the CCEW/MJO relationship. One of the conclusions of that study is that over the Indian Ocean, the amplitudes of all CCEWs except for the MRG are increased in the MJO convective active phase. The discrepancy in the results could be partially due to differences in methodology. For example, we use a grid point variance normalization, as opposed to using the entire record for normalization as *Yasunaga* [2011] did. The differences in approach can be critical for MRGs because the convectively coupled MRG signal-to-noise ratio over the Indian Ocean is very weak [*Dias and Kiladis*, 2014; *Kiladis et al.*, 2016]; therefore, both approaches are particularly sensitive to the background noise. In fact, *Kiladis et al.* [2016] argue that convectively coupled MRGs are primarily confined to the central Pacific sector, which implies that the MRG modulations detected here and perhaps in *Yasunaga* [2011] are due to the background noise.

To further investigate the composition of the MJO, we apply a tracking algorithm that extracts mesoscale contiguous cloudy regions from CLAUS-IR T_b (CCRs). Interestingly, we find that the population of these organized systems within the MJO CE is larger than within MJO SE, but several of their morphological characteristics within MJO CE versus SE remain very similar to climatology. For example, CCR lifetime, size, and phase speeds are not particularly sensitive to the large-scale MJO environment that they are embedded in. In agreement with this finding, there is no global difference between CCR statistics during periods when the MJO is active (OMI A) or inactive (OMI I). While not shown here, we also did not find global CCR sensitivities when they are conditioned on RMM activity. In agreement with the theoretical study by *Moncrieff* [2004], this result suggests that resolving mesoscale systems in GCMs might not necessarily be critical for improving MJO performance.

Finally, our results show that, in agreement with the modulations of low T_b values, the presence of the MJO also increases the amplitude of the T_b diurnal cycle locally. In addition, the diurnal phase distribution in MJO CE is less concentrated during the early morning hours than in climatology, which is in contrast to the more peaked phase distribution associated with suppressed MJO convection. However, on a global scale, the activity of the MJO as measured by the OMI does not affect the T_b diurnal cycle amplitude and phase when integrated over the global tropics. This suggests that more realistic interaction between the MJO and diurnal cycle may lead to locally better representation of them [*Neale and Slingo*, 2003; *Peatman et al.*, 2015], but such improvements should not lead to changes in the global diurnal cycle of precipitation with the MJO. The relationship between the MJO and the diurnal cycle of rainfall and cloudiness, including land and ocean contrasts, is presented in greater detail in *Sakaeda et al.* [2017].

Although many studies have explicitly related the MJO to the activity of specific smaller-scale waves [*Wang*, 1988; *Wang and Rui*, 1990; *Yang and Ingersoll*, 2011, 2013; *Solodoch et al.*, 2011; *Liu and Wang*, 2016], our results imply that beyond the local enhancement in variability, higher-frequency tropical disturbances are not systematically related to the MJO, which suggests that their dispersion characteristics might not be essential for the MJO growth and propagation. Other studies have emphasized the role of smaller-scale disturbances but posit that the details of their structure are not critical [*Majda and Stechmann*, 2009, 2011], which is also at odds with our results in the sense that we did not find a strong local relationship between T_b synoptic variance and MJO amplitude (Figure 7). In contrast, our observational assessment that smaller-scale tropical convection is not systematically affected by the MJO is not in contradiction with the "Moisture Mode" theory [*Sobel et al.*, 2001; *Raymond and Fuchs*, 2009; *Sobel and Maloney*, 2012, 2013], which states that the main processes that control the MJO growth and propagation are related to column-integrated water vapor and the balance among its sources and sinks when integrated across the entire MJO envelope. This planetary-scale moisture-related instabilities share similarities with the large-scale nonrotating convective aggregation phenomena seen in modeling studies such as *Bretherton et al.* [2005] and *Arnold and Randall* [2015]. Interestingly, this view is consistent with our observational result that the MJO tends to redistribute tropical convection geographically without affecting its broader higher-frequency characteristics and global totals.

It is possible that, while not crucial, higher-frequency variability in the makeup of the MJO is related to MJO life cycle stage and propagation characteristics or is more systematically organized across the MJO envelope.

It is also possible that other types of tropical disturbances not included here are more sensitive to the MJO. The authors plan on pursuing these topics, along with investigations of whether the MJO has global impacts in parameters other than rainfall, such as surface temperature. We anticipate that the methodology developed here will be useful in these future studies.

Acknowledgments
We thank Gil Compo and three anonymous reviewers for their thoughtful comments and insights. Naoko Sakaeda acknowledges the support by NRC Research Associate Fellowship. We gratefully acknowledge support for this work through grant NA13OAR4310165 from the Climate Program Office at NOAA. Data are available at http://badc.nerc.ac.uk/view/badc.nerc.ac.uk_ATOM_dataent_claus (CLAUS) and at http://www.cpc.ncep.noaa.gov/products/global_precip/html/wpage.full_res.shtml (Globally Merged IR). We also thank Maria Gehne for producing the CLAUS-IR merged data set.

References

Albright, M. D., E. E. Recker, R. J. Reed, and R. Dang (1985), The diurnal variation of deep convection and inferred precipitation in the central tropical Pacific during January–February 1979, *Mon. Weather Rev.*, *113*(10), 1663–1680.
Arnold, N. P., and D. A. Randall (2015), Global-scale convective aggregation: Implications for the Madden-Julian Oscillation, *J. Adv. Model. Earth Syst.*, *7*(4), 1499–1518.
Benedict, J. J., E. D. Maloney, A. H. Sobel, D. M. Frierson, and L. J. Donner (2013), Tropical intraseasonal variability in version 3 of the GFDL atmosphere model, *J. Clim.*, *26*(2), 426–449.
Bretherton, C. S., P. N. Blossey, and M. Khairoutdinov (2005), An energy-balance analysis of deep convective self-aggregation above uniform SST, *J. Atmos. Sci.*, *62*(12), 4273–4292.
Chen, S. S., and R. A. Houze (1997), Diurnal variation and life-cycle of deep convective systems over the Pacific warm pool, *Q. J. R. Meteorol. Soc.*, *123*, 357–388.
Dias, J., and G. N. Kiladis (2014), Influence of the basic state zonal flow on convectively coupled equatorial waves, *Geophys. Res. Lett.*, *41*, 6904–6913, doi:10.1002/2014GL061476.
Dias, J., S. N. Tulich, and G. N. Kiladis (2012), An object-based approach to assessing tropical convection organization, *J. Atmos. Sci.*, *69*, 2488–2504.
Dias, J., S. Leroux, S. N. Tulich, and G. N. Kiladis (2013), How systematic is organized tropical convection within the MJO?, *Geophys. Res. Lett.*, *40*, 1420–1425, doi:10.1002/grl.50308.
Guo, Y., D. E. Waliser, and X. Jiang (2015), A systematic relationship between the representations of convectively coupled equatorial wave activity and the Madden-Julian Oscillation in climate model simulations, *J. Clim.*, *28*(5), 1881–1904.
Hendon, H. H., and B. Liebmann (1994), Organization of convection within the Madden-Julian Oscillation, *J. Geophys. Res.*, *99*(D4), 8073–8083.
Hodges, K. I., D. W. Chappell, G. J. Robinson, and G. Yang (2000), An improved algorithm for generating global window brightness temperatures from multiple satellite infrared imagery, *J. Atmos. Oceanic Technol.*, *17*(10), 1296–1312.
Huffman, G. J., D. T. Bolvin, E. J. Nelkin, D. B. Wolff, R. F. Adler, G. Gu, Y. Hong, K. P. Bowman, and E. F. Stocker (2007), The TRMM Multisatellite Precipitation Analysis (TMPA): Quasi-global, multiyear, combined-sensor precipitation estimates at fine scales, *J. Hydrometeorol.*, *8*(1), 38–55.
Janowiak, J. E., R. J. Joyce, and Y. Yarosh (2001), A real-time global half-hourly pixel-resolution infrared dataset and its applications, *Bull. Am. Meteorol. Soc.*, *82*, 205–217.
Kikuchi, K., and B. Wang (2008), Diurnal precipitation regimes in the global tropics, *J. Clim.*, *21*, 2680–2696.
Kikuchi, K., and B. Wang (2010), Spatiotemporal wavelet transform and the multiscale behavior of the Madden–Julian oscillation, *J. Clim.*, *23*(14), 3814–3834.
Kiladis, G. N., M. C. Wheeler, P. T. Haertel, K. H. Straub, and P. E. Roundy (2009), Convectively coupled equatorial waves, *Rev. Geophys.*, *47*, RG2003, doi:10.1029/2008RG000266.
Kiladis, G. N., J. Dias, K. H. Straub, M. C. Wheeler, S. N. Tulich, K. Kikuchi, K. M. Weickmann, and M. J. Ventrice (2014), A comparison of OLR and circulation-based indices for tracking the MJO, *Mon. Weather Rev.*, *142*(5), 1697–1715.
Kiladis, G. N., J. Dias, and M. Gehne (2016), The relationship between equatorial mixed Rossby–gravity and eastward inertio-gravity waves. Part I, *J. Atmos. Sci.*, *73*(5), 2123–2145.
Kim, D., A. H. Sobel, E. D. Maloney, D. M. W. Frierson, and I.-S. Kang (2011), A systematic relationship between intraseasonal variability and mean state bias in AGCM simulations, *J. Clim.*, *24*(21), 5506–5520.
Kim, D., A. H. Sobel, A. D. D. Genio, Y. Chen, S. J. Camargo, M.-S. Yao, M. Kelley, and L. Nazarenko (2012), The tropical subseasonal variability simulated in the NASA GISS general circulation model, *J. Clim.*, *25*(13), 4641–4659.
Liebmann, B., and C. Smith (1996), Description of a complete (interpolated) outgoing longwave radiation dataset, *Bull. Am. Meteorol. Soc.*, *77*(6), 1275–1277.
Liu, F., and B. Wang (2016), Effects of moisture feedback in a frictional coupled Kelvin–Rossby wave model and implication in the Madden–Julian Oscillation dynamics, *Clim. Dyn.*, *48*(1–2), 513–522.
Majda, A. J., and S. N. Stechmann (2009), The skeleton of tropical intraseasonal oscillations, *Proc. Natl. Acad. Sci. U.S.A.*, *106*, 8417–8422.
Majda, A. J., and S. N. Stechmann (2011), Nonlinear dynamics and regional variations in the MJO skeleton, *J. Atmos. Sci.*, *68*(12), 3053–3071.
Massey, F. J. (1951), The Kolmogorov-Smirnov test for goodness of fit, *J. Am. Stat. Assoc.*, *46*(253), 68–78.
Masunaga, H., T. S. L'Ecuyer, and C. D. Kummerow (2006), The Madden-Julian oscillation recorded in early observations from the Tropical Rainfall Measuring Mission (TRMM), *J. Atmos. Sci.*, *63*(11), 2777–2794.
Matsuno, T. (1966), Quasi-geostrophic motions in the equatorial area, *J. Meteorol. Soc. Jpn.*, *44*(1), 25–43.
Moncrieff, M. W. (2004), Analytic representation of the large-scale organization of tropical convection, *J. Atmos. Sci.*, *61*(13), 1521–1538.
Nakazawa, T. (1988), Tropical super clusters within intraseasonal variations over the western Pacific, *J. Meteorol. Soc. Jpn.*, *66*(6), 823–839.
Neale, R., and J. Slingo (2003), The Maritime Continent and its role in the global climate: A GCM study, *J. Clim.*, *16*(5), 834–848.
Oh, J.-H., K.-Y. Kim, and G.-H. Lim (2011), Impact of MJO on the diurnal cycle of rainfall over the western Maritime Continent in the austral summer, *Clim. Dyn.*, *38*(5), 1167–1180.
Peatman, S. C., A. J. Matthews, and D. P. Stevens (2014), Propagation of the Madden-Julian oscillation through the Maritime Continent and scale interaction with the diurnal cycle of precipitation, *Q. J. R. Meteorol. Soc.*, *140*(680), 814–825.
Peatman, S. C., A. J. Matthews, and D. P. Stevens (2015), Propagation of the Madden–Julian Oscillation and scale interaction with the diurnal cycle in a high-resolution GCM, *Clim. Dyn.*, *45*(9), 2901–2918, doi:10.1007/s00382-015-2513-5.
Raymond, D. J., and Z. Fuchs (2009), Moisture modes and the Madden-Julian oscillation, *J. Clim.*, *22*(11), 3031–3046.
Roundy, P., and W. Frank (2004), A climatology of waves in the equatorial region, *J. Atmos. Sci*, *61*(17), 2105–2132.
Roundy, P. E. (2008), Analysis of convectively coupled Kelvin waves in the Indian Ocean MJO, *J. Atmos. Sci.*, *65*(4), 1342–1359.
Sakaeda, N., G. Kiladis, and J. Dias (2017), The Diurnal Cycle of Tropical Cloudiness and Rainfall Associated with the Madden–Julian Oscillation, *J. Clim.*, *30*, 3999–4020, doi:10.1175/JCLI-D-16-0788.1.

Sobel, A., and E. Maloney (2012), An idealized semi-empirical framework for modeling the Madden-Julian Oscillation, *J. Atmos. Sci.*, *69*(5), 1691–1705.
Sobel, A., and E. Maloney (2013), Moisture modes and the eastward propagation of the MJO, *J. Atmos. Sci.*, *70*(1), 187–192.
Sobel, A. H., J. Nilsson, and L. M. Polvani (2001), The weak temperature gradient approximation and balanced tropical moisture waves, *J. Atmos. Sci.*, *58*(23), 3650–3665.
Solodoch, A., W. R. Boos, Z. Kuang, and E. Tziperman (2011), Excitation of intraseasonal variability in the equatorial atmosphere by Yanai wave groups via WISHE-induced convection, *J. Atmos. Sci.*, *68*(2), 210–225.
Stechmann, S. N., and A. J. Majda (2015), Identifying the skeleton of the Madden–Julian oscillation in observational data, *Mon. Weather Rev.*, *143*(1), 395–416, doi:10.1175/MWR-D-14-00169.1.
Straub, K. H. (2013), MJO initiation in the real-time multivariate MJO index, *J. Clim.*, *26*(4), 1130–1151, doi:10.1175/JCLI-D-12-00074.1.
Suzuki, T. (2009), Diurnal cycle of deep convection in super clusters embedded in the Madden-Julian oscillation, *J. Geophys. Res.*, *144*, D22102, doi:10.1029/2008JD011303.
Takayabu, Y. N. (1994), Large-scale cloud disturbances associated with equatorial waves. Part I: Spectral features of the cloud disturbances, *J. Meteorol. Soc. Jpn.*, *72*(3), 433–449.
Tulich, S. N., and G. N. Kiladis (2012), Squall lines and convectively coupled gravity waves in the tropics: Why do most cloud systems move westward?, *J. Atmos. Sci.*, *69*(10), 2995–3012.
Wang, B. (1988), Dynamics of tropical low-frequency waves: An analysis of the moist Kelvin wave, *J. Atmos. Sci.*, *45*(14), 2051–2065.
Wang, B., and H. Rui (1990), Dynamics of the coupled moist Kelvin–Rossby wave on an equatorial beta-plane, *J. Atmos. Sci.*, *47*(4), 397–413.
Wheeler, M. C., and H. H. Hendon (2004), An all-season real-time multivariate MJO index: Development of an index for monitoring and prediction, *Mon. Weather Rev*, *132*(8), 1917–1932.
Wheeler, M. C., and G. N. Kiladis (1999), Convectively coupled equatorial waves: Analysis of clouds and temperature in the wavenumber-frequency domain, *J. Atmos. Sci*, *56*(3), 374–399.
Wheeler, M. C., G. N. Kiladis, and P. J. Webster (2000), Large-scale dynamical fields associated with convectively coupled equatorial waves, *J. Atmos. Sci*, *57*(5), 613–640.
Yang, D., and A. P. Ingersoll (2011), Testing the hypothesis that the MJO is a mixed Rossby-gravity wave packet, *J. Atmos. Sci.*, *68*(2), 226–239.
Yang, D., and A. P. Ingersoll (2013), Triggered convection, gravity waves, and the MJO: A shallow-water model, *J. Atmos. Sci.*, *70*(8), 2476–2486.
Yang, G.-I., and J. Slingo (2001), The diurnal cycle in the tropics, *Mon. Weather Rev.*, *129*, 784–801.
Yasunaga, K. (2011), Seasonality and regionality of the Madden-Julian oscillation and convectively coupled equatorial waves, *SOLA*, *7*, 153–156.
Zhang, C. (2013), Madden-Julian oscillation: Bridging weather and climate, *Bull. Am. Meteorol. Soc.*, *94*(12), 1849–1870.